Materials Today Communications 51 (2026) 114918

Contents lists available at ScienceDirect

Materials Today Communications

journal homepage: www.elsevier.com/locate/mtcomm

Tuning radiation attenuation performance of W-substituted nano-$BiNb_{1-x}W_xO_4$ ceramics: A Monte Carlo simulation approach

Rahman I. Mahdi [a], K.A. Mahmoud [b,c], Nabil Janan Al-Bahnam [d], M.H.A. Mhareb [e,f], M.I. Sayyed [g,h,i], Kawa M. Kaky [j,k,*], Usama Altimari [l]

[a] Nanotechnology and Advanced Material Research Center, University of Technology-Iraq, Baghdad 10066, Iraq
[b] Nuclear Materials Authority, P.O. Box 530 El-Maadi, Cairo, Egypt
[c] Ural Federal University, 19 Mira St, Yekaterinburg 620002, Russia
[d] Physics Department, College of Science for Women University of Baghdad, Baghdad, Iraq
[e] Department of Physics, College of Science, Imam Abdulrahman Bin Faisal University, P.O. Box 1982, Dammam 31441, Saudi Arabia
[f] Basic and Applied Scientific Research Center, Imam Abdulrahman Bin Faisal University, P.O. Box 1982, Dammam 31441, Saudi Arabia
[g] Department of Physics, Faculty of Science, Isra University, Amman, Jordan
[h] Renewable Energy and Environmental Technology Center, University of Tabuk, Tabuk 47913, Saudi Arabia
[i] Department of Physics and Technical Sciences, Western Caspian University, Baku, Azerbaijan
[j] Department of Medical Equipment Engineering, College of Engineering Technologies, Al-Nisour University, Baghdad, Iraq
[k] Department of Radiology and Sonography, College of Health & Medical Technologies, Al-Nisour University, Baghdad, Iraq
[l] Department of Medical Laboratory Technologies, College of Health & Medical Technologies, Al-Nisour University, Baghdad, Iraq

ARTICLE INFO

Keywords:
Bismuth-tungsten oxide
Photon-ion attenuation
Stopping power
Lead-free nanomaterials
Proton fluence
High-density compound
Radiation shielding

ABSTRACT

High density ceramics are crucial to next-generation radiation shields because the attenuation of γ- and X-rays scales almost linearly with the atomic number and mass density of the barrier medium. Bismuth and tungsten-based oxides, in particular, can match or surpass lead in stopping power while avoiding its toxicity. This work presents the synthesis of the $BiNb_{1-x}W_xO_4$ solid solution with x = 0, 0.25, 0.50, 0.75, and 1.00 mol% by solid state reaction route. The X-ray diffraction (XRD) shows that the orthorhombic α-$BiNbO_4$ structure changes into the orthorhombic Aurivillius structure when the x value increases. At x = 0.5 mol%, show peak splitting and systematic 2θ shifts, which suggests that a full solid solution has formed instead of only physical mixtures. Fourier-transform infrared (FTIR) spectra show the typical Nb-O and W-O stretching doublets. The average size of the particles in all of the compositions was less than 100 nm. Ion-transport simulations reinforce this promise. The Stopping and Range of Ions in Matter (SRIM) code shows that as the tungsten content increases, the electronic stopping cross-section (SCS) and projected range (PR) of proton energy decrease within an energy range from a few eV to 100 MeV. Damage profiling shows that 5 MeV protons are able to penetrate to a depth of 0.78 mm into $Bi_2W_2O_9$ of 3 mm of the total thickness. These results show that high W content $BiNb_{1-x}W_xO_4$ is highly effective at ion quenching, which supports its application as a high performance, environmentally friendly material for shielding for radiation and particle beams. The Monte Carlo simulation was employed to evaluate the radiation shielding efficacy of $BiNb_{1-x}W_xO_4$ solid solution over the energy range of 0.015–15 MeV. Replacing the Nb ions with W ions significantly enhances the shielding performance of the materials. The linear attenuation coefficient for the prepared samples was increased by 46.81%, 23.06%, and 16.64% at 0.122 MeV, 0.662 MeV, and 1.332 MeV, respectively, when x varied from 0 to 1 mol%. As W ions substitute the Nb ions, the half-value thickness and the equivalent thickness were decreased.

1. Introduction

Protection against harmful radiation is commonly achieved using lead, concrete, or heavy metal glasses; however, these traditional materials are content poisonous, fragile, or challenging to incorporate into sophisticated electronics. Due to its high atomic number and low toxicity bismuth is considered a solid, environmentally friendly option that offers substantial photoelectric cross sections without the negative

* Corresponding author at: Department of Medical Equipment Engineering, College of Engineering Technologies, Al-Nisour University, Baghdad, Iraq.
E-mail address: kawa.mudher@gmail.com (K.M. Kaky).

https://doi.org/10.1016/j.mtcomm.2026.114918
Received 8 July 2025; Received in revised form 23 January 2026; Accepted 24 February 2026
Available online 27 February 2026

environmental impacts associated with lead [1–4]. Bismuth based materials have received significant attention in various fields, such as radiation shielding, photocatalysis, and energy storage, among others [5–9]. Among them, bismuth niobate $BiNbO_4$ has received significant interest in microwave dielectrics, piezo, ferroelectrics, and visible-light photocatalysis because the Bi-6s/O-2p hybridization lowers its bandgap and the Nb-4d orbitals speed up charge transfer [6,10–16]. The material crystallizes into two phases, an orthorhombic α-$BiNbO_4$ (*Pnna*) and a triclinic β-$BiNbO_4$ (*P*1) that. Both phases are constructed from corner sharing (NbO_4) tetrahedra and distorted Bi-O layers. These results in a dense three dimensional network that exhibits mechanical durability and chemical stability [17,18]. The theoretical density of $BiNbO_4$ is around 7.5 g cm^{-3} , and conventional sintering methods can reach up to 96% of the theoretical density with an experimental density of about 7.2 g cm^{-3} . This value is already equivalent to commercial lead glass shields [19,20].

The valent substitution of Nb^{5+} ion with an atomic mass of 92.9 u with the considerably heavier W^{6+} ion with an atomic mass of 183.8 u, can lead to enhance the density of $BiNbO_4$, and this is expected to enhance radiation attenuation capability. The density of tungsten with 19.3 g cm^{-3} and its atomic number Z = 74, adds more photoelectric centers and Compton scatterers. Its 5d orbitals also make Bi-O-W more covalent, which makes the lattice stronger and more resistant to high flux radiation over the years [13]. It has been reported that a layered crystal structure, $Bi_2(W_{1-x}Mo_x)O_6$, by replacing the bismuth with tungsten, the density increases from 8.15 to 9.50 g/cm^3 and steadily increases the linear attenuation coefficient across the evaluation energy range [21]. It is expected that the same approach should work even better in the denser scheelite structure of the $BiNb_{1-x}WxO_4$ system. But except for a few qualitative diffraction investigations on very low W concentrations, the overall impact of total Nb to W substitution on the shielding characteristics of Bi-niobates remains unexplored.

The corner sharing (Nb/W)O_4 tetrahedra in scheelite-type $BiNb_{1-x}WxO_4$ establish linear, densely packed diffusion pathways that enhance multiple photon–electron interactions and reduce internal porosity. The stereochemically active 6 s^2 lone pair on Bi^{3+} concurrently induces local lattice deformation, enhancing phonon scattering and facilitating the dissipation of heat created by high-energy beams [10,22,23]. The $BiNb_{1-x}WxO_4$ system with its unique compact structure, a high effective atomic number, and superior thermal and mechanical properties, makes a potential candidate for lead-free radiation shielding materials [21,24,25].

In this work, we focus on the synthesis of $BiNb_{1-x}WxO_4$ with x values of 0, 0.2, 0.5, 0.75, and 1. The crystalline structure, vibrational spectroscopy, particle size, surface area, charged stopping power, and capability to block radiation were comprehensively explored. The SRIM-2013 Monte Carlo is used to determine the electronic energy loss function and the stopping power. Gamma-ray shielding performance was estimated using MCNP-5 transport simulations and the ENDF/B-VI.8 nuclear data library. MCNP-5 simulations of photon paths within customized geometries provide key shielding parameters, including the linear attenuation coefficient (LAC), mass attenuation coefficient (MAC), half-value layer (HVL), and radiation protection efficiency (RPE) [26–29]. The experimental results and theoretical simulation link fundamental materials physics with effective strategies for radiation shielding. The understanding gained enables the formation of structures that incorporate crystallographic density W enhanced Z_{eff}, and the advantageous chemistry of bismuth to meet the gradually increasing high safety and sustainability standards of nuclear medicine, aerospace equipment, and clean energy facilities.

2. Materials and methods

2.1. Preparation and characterization of $BiNb_{1-x}W_xO_4$

The $BiNb_{1-x}W_xO_4$ solid solutions (x = 0, 0.25, 0.5, 0.75, and 1) were prepared by a solid-state approach. Stoichiometric amounts of Bi_2O_3, 99/9% (80 nm, Sigma Aldrich, Germany), Nb_2O_5 99/9% (50 nm, American Elements, USA), and WO_3 99/9% (60 nm, US Research Nanomaterials, USA) were carefully mixed in ethanol and subjected to ball milling for 10 h using a ball mill grinding machine to achieve homogeneity. The obtained powder was then dried at 100 °C for 10 h to remove the ethanol. The resulting powder has been calcined at 900 °C for 4 h at a ramping rate of 6 °C/min, resulting in the formation of the $BiNb_{1-x}W_xO_4$. The powders were further milled for 20 h after calcination to break up agglomerates and refine particle size for characterization. The crystalline structure was evaluated by X-ray diffraction (XRD, Empyrean PANalytical, Holland) over 2θ = 5°–70° (0.01° step), with target Cu K*α* radiation, λ= 1.5405 Å, voltage 40 kV, and current 30 mA allowing identification of crystalline phases and lattice shifts due to W substitution. To identify the phases in $BiNb_{1-x}W_xO_4$, we used Crystal Impact Match (Match3) software to compare the observed profiles to reference entries and choose the most consistent phase assignment and space group. The software's Scherrer-type peak-broadening tool was also used to estimate crystallite size. An IRTracer-100, Shimadzu, Japan, Fourier transform infrared spectroscopy (FTIR), in the 2000–400 cm^{-1} range, identified vibrational modes. The $BiNb_{1-x}W_xO_4$ particle size has been examined using Malvern Panalytical Mastersizer 3000 + . The stopping power, mean excitation potential I(eV), and proton damage disruption of $BiNb_{1-x}W_xO_4$, have been estimated by three free software SRIM, CasP (Convolution approximation for swift Particles) version 6.0, and SUSPRE (Stopping power for Ultra-Slow Particles in real solids), respectively to describe energy loss and parameterizations of the dielectric target for each molar ratio x. On the other hand, MCNP-5 transport simulations and the ENDF/B-VI.8 nuclear data library were used to determine the effectiveness of gamma-ray shielding.

2.2. Evaluation of γ-ray shielding parameters

The Synthesized $BiNb_{1-x}W_xO_4$ composites were examined for shielding efficacy at γ-ray energy ranging from 0.015 to 15 MeV using the Monte Carlo N-Particle (MCNP-5) transport code [30]. The most crucial step in the simulation procedure was establishing the average track length (ATL, cm) of γ-rays over synthetic $BiNb_{1-x}W_xO_4$ composites. To estimate the ATL of γ-ray across the cell containing $BiNb_{1-x}W_xO_4$ composites, the photon tally card was set to F4 in the input file. The input file also contains materials, cutoff, tally, cell, surface, and source (SDEF) card data. The evaluation approach used interaction cross-sections (σ) from the nuclear database ENDF/B-VI.8, which is linked to the MCNP-5 code. The input file describes the simulation geometry, which consists of a large, evacuated lead cylinder that protect the detector from background radiation. The lead cylinder is 40 cm tall and 17.5 cm radius. The position of the radioactive source is POS (0 0 0) in the lead cylinder which means that the radioactive source was located at the center. The photons emitted from the radioactive source in all directions toward +Z direction with AXS (0 0 1). The emitted radiation is described as (PAR: 2) to confirm that the radioactive source emits a monoenergetic. The energy of these photons was introduced in the input file, where the simulation process was performed over a wide energy interval varied from 0.015 to 15 MeV to cover wide range of γ-ray energies. These photons were collimated with a 7-cm-tall, 2.5-cm-radius collimator with a central narrow slit which has a radius of 0.5 cm. The cylindrical shaped $BiNb_{1-x}W_xO_4$ composites receives perpendicular photons that are directed from the first collimator. A second collimator collimated photons after interaction with the $BiNb_{1-x}W_xO_4$ samples and directed it toward the detector. The cutoff card's NPS ceased photon emissions after 10^6 historical. The high historical emission was selected to decrease the relative error in the simulated ATL to the lower levels. After completing the simulation, a new output file is generated with a relative error in the ATL dropped to ±0.15%.

To determine the linear attenuation coefficient (LAC, cm) which considered the main critical shielding parameter for any material, Eq.

(1) was used to calculate it based on the average flux per unit cell containing the $BiNb_{1-x}W_xO_4$ composites.

$$LAC(cm^{-1}) = \left(\frac{1}{x}\right)\ln\left(\frac{I_o}{I_t}\right) \quad (1)$$

I_o and I_t represent the average photon flux before and after interaction with the cell containing the $BiNb_{1-x}W_xO_4$ composites. Half Value Layer (HVL, cm) represents the thickness of $BiNb_{1-x}W_xO_4$ composites. which decreases the transmitted photons (I_t) by 50% of its initial value (I_o). It is reversely proportional to the LAC of prepared $BiNb_{1-x}W_xO_4$ composites, as illustrated in Eq.(2).

$$HVL(cm) = \frac{\ln(2)}{LAC} \quad (2)$$

It is known that at hospitals they used protective lead rubber jackets with lead thickness varying between 0.025 and 0.05 cm for personal protection against X-rays or γ-rays. In the current work, the thickness of the prepared composites, which have similar shielding capacity as 0.05 cm of Pb, is known as the thickness equivalent lead (TEL, cm). It can be calculated for the synthesized $BiNb_{1-x}W_xO_4$ composites based on the It and Io for both the synthesized $BiNb_{1-x}W_xO_4$ composites and pure lead, as presented in Eq. (3).

$$LET(cm) = \frac{\left(\ln\left(\frac{I_o}{I_t}\right)\right)_{Lead}}{\left(\ln\left(\frac{I_o}{I_t}\right)\right)_{composite}} \quad (3)$$

The radiation protection efficiency (RPE, %) describes the amount of photons that are absorbed within the synthesized $BiNb_{1-x}W_xO_4$ composites as a result of the interaction of photons with the electrons inside the material. The RPE for the synthesized $BiNb_{1-x}W_xO_4$ composites can be calculated according to Eq. (4).

$$RPE(\%) = \frac{I_o}{I_a} = \left(1 - \left(\frac{I_o}{I_t}\right)\right) \times 100 \quad (4)$$

3. Results and discussion

3.1. Crystal structure and phase identification of $BiNb_{1-x}W_xO_4$

Fig. 1 illustrates the XRD of $BiNb_{1-x}W_xO_4$ at varying x, demonstrating the progression of crystalline phases as tungsten replaces niobium, as illustrated in Table 1. As W content increases from x = 0 to x = 1, the diffraction patterns exhibit qualitative alterations indicative of a transition from Orthorhombic β-$BiNbO_4$ phase to Orthorhombic γ-Bi_2WO_6 phase. At x = 0 (absence of W), all peaks belong to $BiNbO_4$, namely the orthorhombic α-$BiNbO_4$ phase, which is well indexed with the standard XRD pattern JCPDS No. 01–082–0348 [22]. This phase is distinguished by prominent reflection peaks at 2θ, 15.11, 23.76, 28.28,30.50, 31.51, 32.45, 35.12, 36.05, 44.42, 47.92, 52.85,54.15, 58.49, 60.16, 61.19, and 67.95 among other peaks [8]. In the doped sample with x = 0.25, the XRD pattern is predominantly characterized by $BiNbO_4$ peaks, showing only minor alterations, slight peak displacements to higher 2θ (indicative of a smaller W^{6+} ion partially substituting Nb^{5+} in the lattice), and peak broadening, suggesting that W is incorporated into the $BiNbO_4$ structure as a solid solution. No additional distinguishable peaks emerge at x = 0.25, indicating that the solid solubility of W within the $BiNbO_4$ lattice has not been exceeded. At x = 0.5, additional weak reflections begin to appear alongside the $BiNbO_4$ peaks. The emergence of these additional peaks indicates the development of a secondary tungsten-rich phase when the tungsten concentration reaches a substantial level. The predominant reflections of $BiNbO_4$ persist, suggesting that $BiNbO_4$ remains the principal phase at x = 0.5; nevertheless, the emergence of new peaks (notably a minor peak around 2θ ≈ 29–30° and other peaks at elevated angles) suggests the incipient crystallization of a bismuth tungstate phase. At x = 0.75, the XRD pattern indicates a

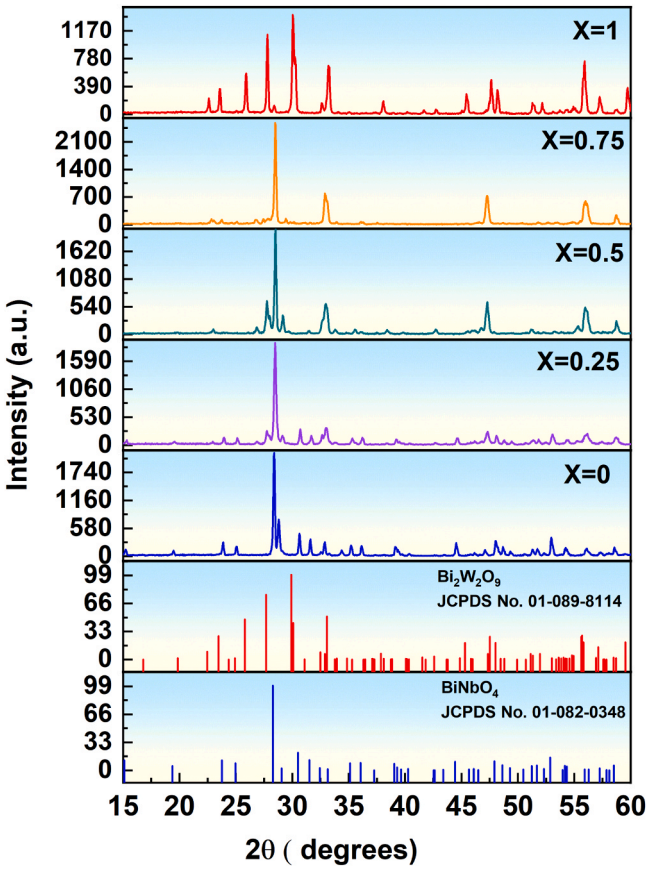

Fig. 1. The XRD pattern of $BiNb_{1-x}WxO_4$ at different x.

distinct two-phase combination. The peaks of $BiNbO_4$ have significantly diminished in relative strength, while the peaks of the tungsten-containing phase have grown pronounced. Numerous distinct reflections, typical of bismuth–tungsten oxide, emerge across the 2θ spectrum, notably prominent peaks in the ~28–33° range and supplementary peaks at higher angles. This indicates that a substantial fraction of the sample has transformed into a bismuth tungstate phase, with residual $BiNbO_4$ present as a minor component. In the $BiNb_{1-x}W_xO_4$ structure, it is not possible to totally replace Nb with W to form the $BiWO_4$ structure at x = 1, instead of the formation of $Bi_2W_2O_9$, rather than $BiWO_4$. This can be explained through analysis of charge equilibrium and structural strength. Bi ion is generally trivalent Bi^{3+} in these oxides, while W is commonly hexavalent W^{6+}. A theoretical $BiWO_4$ structure would have Bi^{3+} and W^{6+}, which would be balanced by O^{2-}. This will give it a total cation charge of + 9, which 4 O^{2-} (–8 charge) cannot completely balance [31]. $Bi_2W_2O_9$, on the other hand, has a Bi:W ratio of 1:1 and nine oxygen atoms per formula unit. This means that $Bi_2W_2O_9$ may be represented as $Bi^{23+} + 2\,W^{6+} = +18$, with nine $O^{2-} = -18$. $Bi_2W_2O_9$ maintains neutral in terms of charge, but $BiWO_4$ has insufficient electrons. The confirmed binary Bi_2O_3-WO_3 phase diagram demonstrates the chemical reality. The stable bismuth tungstate phases include Bi_2WO_6 and $Bi_2W_2O_9$, as well as higher members like $Bi_2W_3O_{12}$. However, there is no document of a simple Bi: W: O = 1:1:4 phase in mainstream databases [32–34]. As x approaches 1 the additional W promotes the formation of the orthorhombic phase, identified by the *Pna*21 space group of $Bi_2W_2O_9$, which is accurately indexed by JCPDS No. 01–089–8114 [35], as confirmed by the XRD results. Further analysis was carried out to identify the phases and estimate the crystallite size. The XRD patterns of $BiNb_{1-x}W_xO_4$ show broad peaks which are consistent with nanocrystalline domains. Because this broadening, together with the modest counting statistics, makes a full Rietveld refinement weakly constrained and sensitive to correlated fitting terms

Table 1
Main phase, lattice parameters volume and crystalline size of fabricated samples.

Sample code	Main phase and space group	a (Å)	b (Å)	C (Å)	V (Å)^3	Crystalline size (nm)
0	***Pnna* Orthorhombic β-$BiNbO_4$**	4.983	11.704	5.681	331.4	81
0.25	***Pnna*** orthorhombic β-$BiNbO_4$ structure	4.967	11.680	5.667	329.0	101
0.5	***Pnna* Orthorhombic** β-$BiNbO_4$	4.952	11.655	5.652	326.2	90
0.75	***Pca*21 Orthorhombic** Bi_2WO_6	5.457	16.473	5.438	488.7	101
1	*Pca*21 **Orthorhombic γ-$Bi_2W_2O_9$**	5.457	16.427	5.438	487.7	78

such as background, peak-shape, and size or strain broadening, we did not report refined lattice parameters. Instead, we used Crystal Impact software to identify the main phase and the most consistent space group by reference matching, and we present a Scherrer type crystallite size estimate as an approximate supporting value. The identified phases are orthorhombic *Pnna* for x = 0, 0.25, and 0.50, while at higher W contents above x = 0.50 the phase is assigned as orthorhombic *Pca21*, as summarized in Table 1.

3.2. Vibrational modes and local bonding of $BiNb_{1-x}W_xO_4$ by FTIR spectroscopy

Fig. 2 shows the FTIR results of $BiNb_{1-x}W_xO_4$. As the W content rises from 0 to 1 mol%, the FTIR spectra show clear differences in peak position and the formation of new bands, confirming changes in chemical bonding with increasing x value. At x = 0, the peak at about 820 cm^{-1} is attributed to the stretching of Bi-O-Bi modes, and the peak at 620 cm^{-1} is assigned to Nb-O-Nb stretching. The peak at 500 cm^{-1} associated with

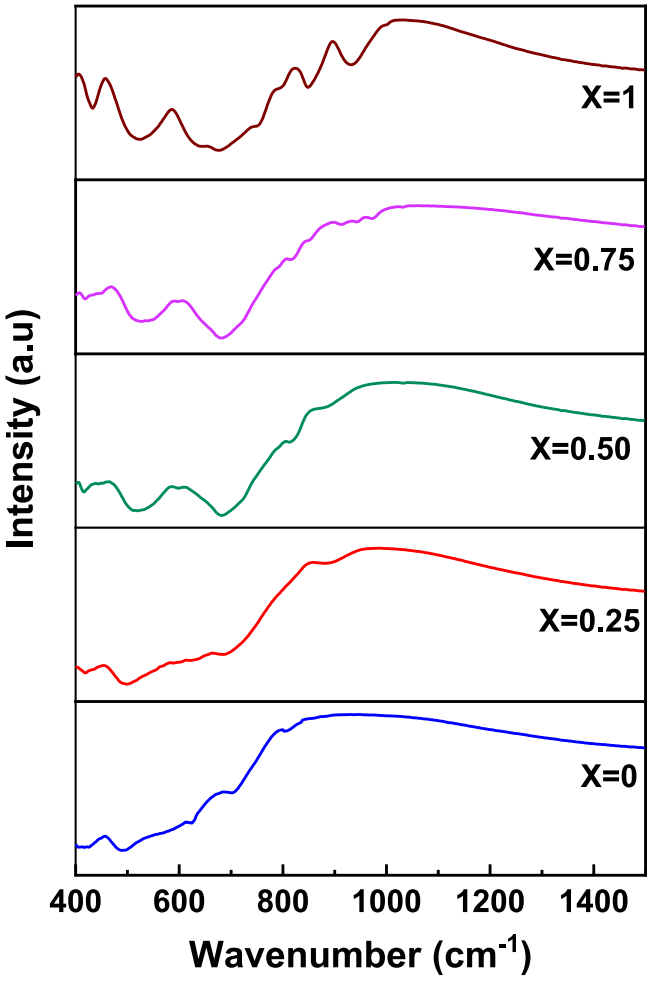

Fig. 2. FTIR spectra of the $BiNb_{1-x}W_xO_4$.

bending vibrations involving Bi-O/Nb-O bonds in the niobate structure, all peaks confirm the formation of the $BiNbO_4$ structure [36–38]. Further increases in x value to x = 0.25 and 0.5 result in the FTIR peaks shifting and developing due to the incorporation of W-O bonds. Tungsten is heavier element and often forms stronger bonds, so its stretching modes appear in similar frequency regions but can alter the spectrum noticeably. For instance, the peak at 820 cm^{-1} Bi-O-Bi band broadens slightly shifts toward 800 cm^{-1} as W is introduced, indicating the contribution of W-O stretching modes overlapping in that region. At the same time, the Nb-O-Nb peak at 620 cm^{-1} decreases in strength as Nb concentration decreases. A shoulder appears in the 700–640 cm^{-1} range, indicating W-O-W bridging stretches in corner sharing WO_6 octahedra. As the x increases to 0.75 mol%, a new band forms at about 870 cm^{-1} , showing that tungsten is in octahedral coordination (WO_6). The increase in bandwidth at 500 cm^{-1} is due to the bending modes of heavy metal oxygen polyhedra, particularly the deformation of WO_6 octahedra and Bi-O units in the shifting lattice. A partial transition from $[WO_4]^{2-}$ tetrahedral to WO_6 octahedral is observed [39–41]. With further increase in W content to x = 1 mol%, the results indicated formation of $Bi_2W_2O_9$. The peak at 850 cm^{-1} corresponds to the asymmetric stretching of WO_6 octahedra, while the peak at 936 cm^{-1} is attributed to vibrations of short W-O bonds [39]. Overall, XRD and FTIR were used to test the experiment and confirm that the phases were forming and that no secondary phases were present that could alter the composition assumed in the material specification. The FTIR spectra confirmed the expected bonding properties and showed no clear signs of significant residual precursors or impurities. Despite the XRD and FTIR results not directly used in the numerical simulations, they serve as important proof that the composition assumed in the simulation material specification is accurate.

3.3. Dispersion state and hydrodynamic diameter of $BiNb_{1-x}W_xO_4$

Fig. 3 illustrates the particle size analysis (PSA) of $BiNb_{1-x}W_xO_4$ across various x values ($0 \leq x \leq 1$). All powders were diluted with ethanol to suitable proportions to provide a clear solution, and subsequently subjected to probe sonication for 2 min at 50 watts to achieve optimum dispersion [15]. Each test was conducted four times, with each run lasting 15 s under motion, after which the average was calculated. At x = 0, the histogram (Fig. 3**a**) exhibits a narrow, almost normal distribution centred about 80 nm, ranging from 70 to 90 nm. The introduction of 25 mol% W (Fig. 3 **b**) moves the distribution towards smaller diameters, resulting in a new mean of around 75 nm, with a minor widening of the range to 60–90 nm, indicating that partial W-substitution facilitates moderate grain refinement. The tendency is particularly evident at x = 0.50 (Fig. 3**c**). The particles reach a maximum size of around 65 nm, with a broad range of 45–85 nm, resulting in the lowest average diameter in the series. As the W content increases, growth declines, x = 0.75 (Fig. 3**d**) shows a mean of around 85 nm, while totally replaced x = 1 (Fig. 3**e**) reaches 95 nm.

Fig. 3f illustrates the specific surface area (SSA) of $BiNb_{1-x}W_xO_4$ at different x values ($0 \leq x \leq 1$). The blue curve validates a non-monotonic diameter profile of 80 nm, 73 nm, 65 nm, 85 nm, and 95 nm as x increases from 0 to 1. The black curve illustrates the inverse progression of specific surface area about 9, 10.3, 11.7, 7.9, and 7.2 $m^2\ g^{-1}$, respectively. The traditional 1/d ratio indicates that a diameter reduction to

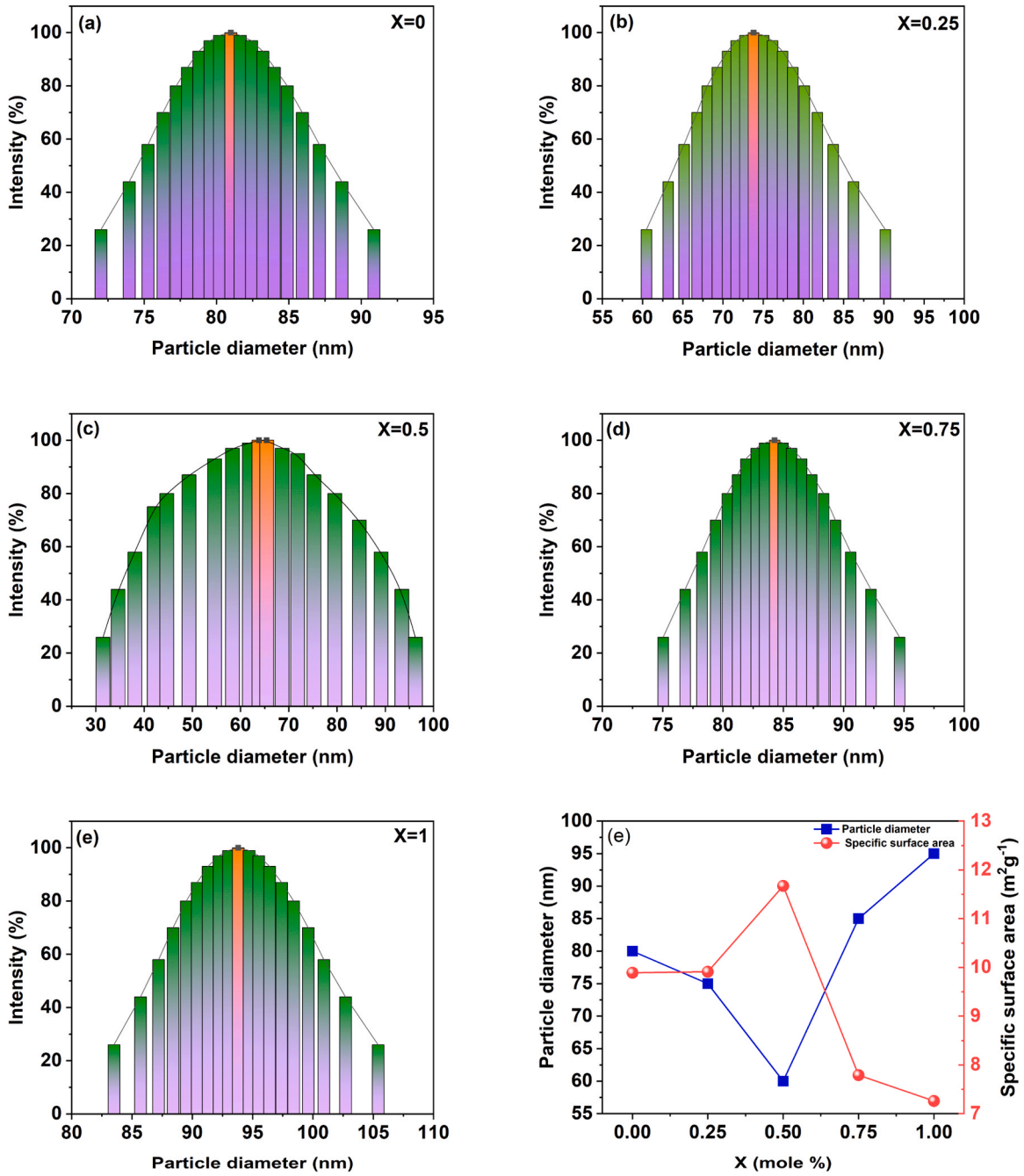

Fig. 3. The particle-size histograms for $BiNb_{1-x}W_xO_4$ (a-e) for x = 0, 0.25, 0.50, and 0.75, respectively, and (f) demonstrates the specific surface area and mean diameter of particle size at different x values.

x = 0.50 results in almost twice the specific surface area compared to the original phase.

3.4. *Effect of $BiNb_{1-x}W_xO_4$ composition on stopping ions and projected range*

The stopping cross-section (SCS) and projected range (PR) of $BiNb_{1-x}W_xO_4$ for H, He, Be, C, O, and Ne have been evaluated using the SRIM software package [42]. Bragg's additivity rule (BAR) plays a major role in the SRIM software when computing the SCS and projected range of ions in compounds or stoichiometric materials. According to BAR, the sum of the energy losses a projectile would experience if it were traveling through each element, weighted by their respective ratios, can be used to approximate the total SCS (i.e., total energy loss per unit distance) of the projectile passing through a mixture or compound. The SCS and PR are important quantities in radiation physics because they demonstrate the correlation between the energy loss of ions and stopping medium excitations. Figs. 4 and 5 represent the SCS and PR of protons in $BiNb_{1-x}W_xO_4$, examined in the energy range of T(MeV) up to 100 MeV with different molar ratios (where x = 0, 0.25, 0.5, 0.75, and 1). From the computations, it is evident that the SCS and PR values start to increase from 1 eV and 1 Å, respectively. Beyond these values, the SCS data decrease, while PR reaches a maximum value. Clearly, changes in the energy losses occur around the stopping maxima, and the SCS of the $BiNb_{1-x}W_xO_4$ samples follows the order; $SCS_{x=0} > SCS_{x=0.25} > SCS_{x=0.5} > SCS_{x=0.75} > SCS_{x=1}$. Meanwhile, the RP follows the order: $(PR=17.5\ mm)_{x=0} > (PR=16.8\ mm)_{x=0.25} > (PR=16.21\ mm)_{x=1} > (PR=16.11\ mm)_{x=0.5} > (PR=15.5\ mm)_{x=0.75}$ at 100 MeV. Energy loss

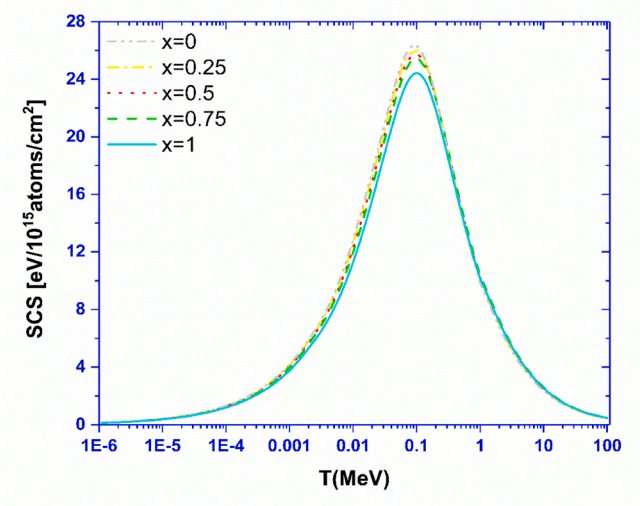

Fig. 4. The electronic SCS for protons in $BiNb_{1-x}W_XO_4$ (x = 0, 0.25, 0.5, 0.75, and 1).

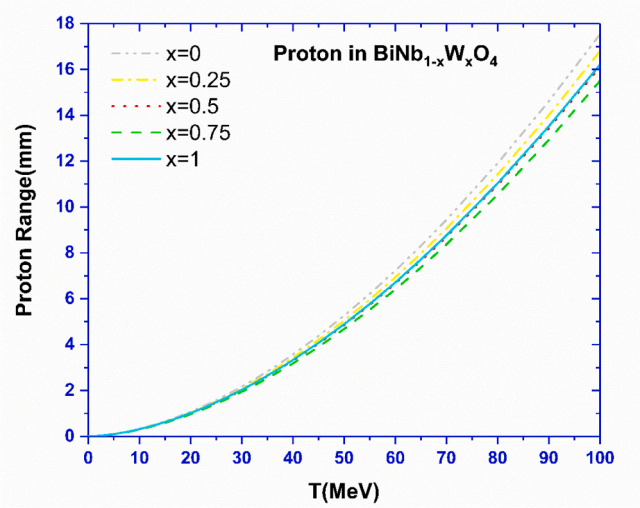

Fig. 5. PR for proton in $BiNb_{1-x}W_xO_4$ (x = 0, 0.25, 0.5, 0.75, and 1).

and range are strongly dependent on the concentration of tungsten, and the best results for proton radiation shielding were obtained for concentrations between $0.5 \leq x \leq 1$, due to the lowest projected ranges in those ratios. In the same context, the PR values tend to decline with increasing tungsten molar mass concentration because the density of tungsten is greater than that of Bi, Nb, and O. Therefore, these increments reflect higher density (except x = 1), leading to significant proton interactions with atomic electrons in the $BiNb_{1-x}W_xO_4$ compound. Theoretically, as W increasingly replaces Nb, it might induce a change in the electronic structure of $BiNb_{1-x}W_xO_4$, increasing electron density or varying the distribution of free electrons, which improves electronic SCS results. Our computations showed a progressive decrease in stopping values with increasing concentration. This is due to polarization effects and density corrections of the target material [43]. Polarization effects indicate how the electronic cloud around atoms or ions in the $BiNb_{1-x}W_xO_4$ compound deforms in response to the dynamic movement of protons. A highly polarizable medium can expedite the redistribution of its electronic density, which can boost or adjust energy transfer processes [4,44–47]. Conversely, if the polarization effects are reduced or suppressed due to modifications in the $BiNb_{1-x}W_xO_4$ structure composition, the SCS may decrease, as shown in Fig. 4. Subsequently, the density effect correction modifies the energy loss data, indicating that polarization reduces energy transfer at high energy ranges, leading to precise predictions of ion projected ranges and energy deposition profiles. Electronic SCS dominates for proton energies exceeding a few hundred keV. The electron density significantly influences the sensitivity of the $BiNb_{1-x}W_xO_4$ target, the effective charge of the proton, which is diminished due to the screening effect, and the shell structure of $BiNb_{1-x}W_xO_4$ atoms, particularly at low proton energy. Atomic target electrons screen the nuclear charge at energy levels below T = 10 MeV, therefore lowering Coulomb interactions and hence the effective nuclear charge of the projectile (Zeff), and hence reducing energy loss at low energies. Realistic projections of projectile range and stopping power matched with experimental observations are obtained by use of these SRIM software modifications. Furthermore, inelastic electron mean free path (IMFP) data is used in computerized modeling, such as Monte Carlo (MC) simulations, to probabilistically locate where inelastic collision events occur along an ion's track, thus affecting expected energy loss and projected range in condensed media. Since the IMFP relates to electronic relaxation time, damping, and energy dissipation processes [48], it influences dielectric response qualities. These results align with those of Chaiphaksa et al. [49], when they found that the Gd_2O_3 concentration in the bismuth borate glass (80-x) B_2O_3:5CaF_2:15Bi_2O_3:xGd_2O_3 reduced the energy loss and range of proton and alpha particle as the molar ratio x changed from 0% to 20%, due to the increased density of the material.

3.5. Prediction of proton bragg peak profiles in $BiNb_{1-x}W_xO_4$

Experimental data for SCS are frequently available for individual components, although they are currently lacking for complex dielectric materials. The SRIM algorithm uses Bragg's additivity rule to predict the total energy loss and range of the compound. The International Atomic Energy Agency (IAEA) provides a reliable, standardized database on various charged particles such as protons, alpha particles, and heavy ions, including the stopping power of different materials. In Fig. 6, a comparative analysis of five $BiNb_{1-x}W_xO_4$ samples (where x = 0, 0.25.0.5, 0.75, and 1) is presented along with the individual elements of the compound Bi, Nb, W, and oxygen. The stopping experimental data adheres to the IAEA SCS database terminology for naming or labeling, which associates the authors' surnames with the publication year.

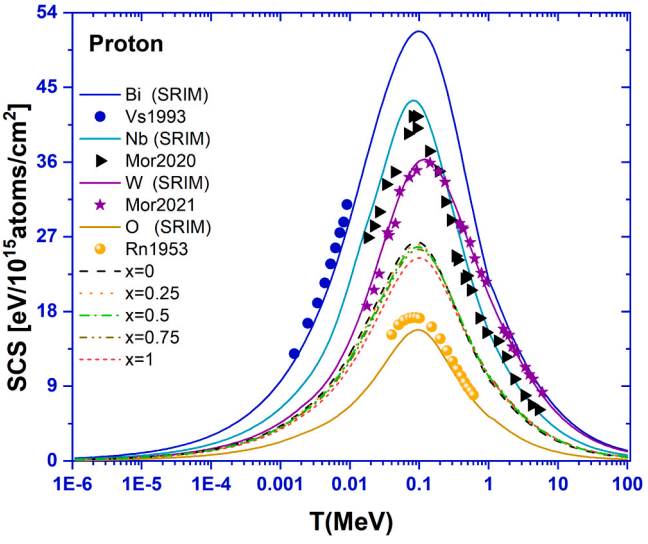

Fig. 6. Electronic stopping cross section (SCS) of protons in $BiNb_{1-x}W_xO_4$ (x = 0, 0.25, 0.5, 0.75, and 1) as a function of proton energy, T (MeV). Symbols denote experimental values retrieved from the IAEA database for single-crystal targets, while solid lines correspond to theoretical results calculated using the SRIM code.

For protons moving in Bi, Nb, W, and O, the SRIM code prediction shows good coherence with the experimental data stopping values spanning the following energy ranges: 1.59 keV <T ≤ 9 keV reported by Valdés et al. [50] (Vs1993) for the Bi target, 18 keV <T < 5.2 MeV obtained by Moro et al. [51] (Mor2020) for the Nb target, 17 keV <T < 6 MeV measured by Moro et al. [52] (Mor2021) for the W target, and 40 keV ≤ T < 0.6 MeV provided by Reynolds et al. [53] (Rn1953) for the oxygen target in the gas phase. Through the experimental individual contributions of elements concerning electronic stopping, the SRIM software can anticipate how the Bragg peak's position alters with different molar ratios and determine the changes in energy loss distribution with target density. This leads to an increase in the reliability of the expected stopping results for the $BiNb_{1-x}W_xO_4$ samples, especially when there is inadequate data available about the proposed compounds; here, the BAR would be the best choice method.

Figs. 7**a** and 7**b** show the calculation of mean excitation potential I (eV) and bulk plasmon $E_{Bulk} = \hbar\omega_p$ for fabricated $BiNb_{1-x}W_xO_4$ samples (distributed over each molar ratio) alongside the pure elements of their components. The mean excitation potential for the synthesized samples was determined using the convolution approximation for swift particles (CasP) program, version 6 [54].

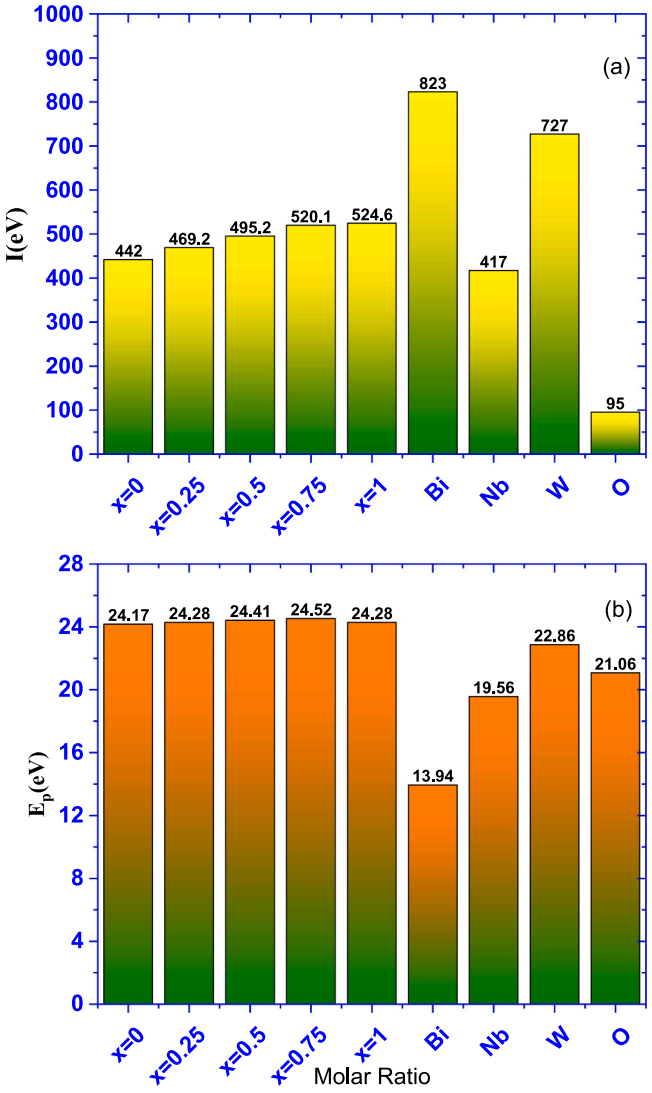

Fig. 7. The target computations for: (a) The mean excitation potential I(eV) for $BiNb_{1-x}W_xO_4$ (x = 0, 0.25, 0.5, 0.75, and 1) compared with the single solid target based on CasP computations. (b) The bulk plasmon for $BiNb_{1-x}W_xO_4$ (x = 0, 0.25, 0.5, 0.75, and 1) compared with the single solid target based on Eq. (5).

In a stopping material, the mean excitation potential is the average energy required to excite or ionize an atom. It is an essential factor in approximating electronic energy loss using methods such as the Bethe formula. It significantly affects the logarithmic term, controlling the energy loss rate at decreasing projectile energies when the logarithmic term $\mathrm{Ln}\langle I\rangle$ becomes progressively essential. Accurate energy loss computations rely on precise calculations of particle energy loss [55].

Swapping Nb with W leads to an increase in mean excitation potential values of the $BiNb_{1-x}W_xO_4$ samples. This increase may arise from various factors related to the atomistic and electronic structure properties of W compared to Nb. Tungsten has a higher atomic number (Z) than Nb, and elements with high Z usually exhibit a larger effective nuclear charge, including more tightly bound inner electrons, higher excitation potentials, and average ionization energies, which contribute to the increase in average effective nuclear charges in the lattice. This increases I-values by excitation or elimination of atomic electrons, requiring additional energy. The electronic configuration and orbital effects indicate that higher energy is needed for excitation, as W has extra f electrons and higher energy d orbitals, which promote a more complicated and stabilized electronic structure. It should be noted that the strong W-O bonding changes the electronic band structure and modulates the crystal field strength, thus improving the I-values of the samples [56,57]. In addition, the dipole oscillator strength distribution or oscillator strength density shifts to higher energies owing to tungsten's heavier atomic nature. Besides the atomic electrons being bound tightly, causing a change in the logarithmic mean energy, resulting in an upward rising I value [58,59], as shown in Fig. 7a. We conducted bulk plasmon energy calculations for all shields to gain a deeper understanding of the relationship between plasma frequency and projectile energy loss in complex media. Plasmon excitations are collective oscillations of electrons of the target material.

The characteristic of bulk plasmon energy E_p, depends on the electronic structure nature and density ρ of the material [60,61]. In compounds, the E_p can be read as

$$E_P = 28.816\sqrt{\sum_i \frac{N_{V,i}\rho_i}{M_i}} \quad \text{.....} \tag{5}$$

Where $N_{v,i}$, ρ_i, M_i are the valence electrons, density(gm/cm^3), and atomic mass of single element i.

Fig. (7**b**) shows the E_p values of single elements along with fabricated $BiNb_{1-x}W_xO_4$ samples. When an element composes a $BiNb_{1-x}W_xO_4$ compound, its atomic electrons interact and delocalize over the whole structure, producing a new collective behavior mode that is different from those in a single element. Hybridization and bonding lead to an effective enhancement of free or delocalized electron density compared to single elements. The penetrating charged particles induce a reorganization of atomic electrons in the dielectric target, resulting in localized variations in electronic density. These induced densities are closely linked to the wake or induced potential; they consider how atomic electrons collectively react through plasmons and screening to the moving ion [62]. Knowledge of this relationship between E_p, I, SCS, and PR aids in optimizing $BiNb_{1-x}W_xO_4$ for nuclear radiation detection measurements, such as detector design and radiation shielding, by tailoring their electronic characteristics to achieve the desired energy loss properties.

3.6. Swift heavy ion stopping power and projected range in $BiNb_{1-x}W_xO_4$ at high tungsten content (x = 0.75, 1)

The current section focuses on the behavior of swift heavier ions in interaction with $BiNb_{0.25}W_{0.75}O_4$ and $Bi_2W_2O_9$, as they have the lowest projected range among the other samples, as illustrated in Fig. 5.

Figs. 8 and 9 show the SCS and PR results of H, He, Be, C, O, and Ne ions striking $BiNb_{1-x}W_xO_4$ elevated at high tungsten concentrations, i.e.,

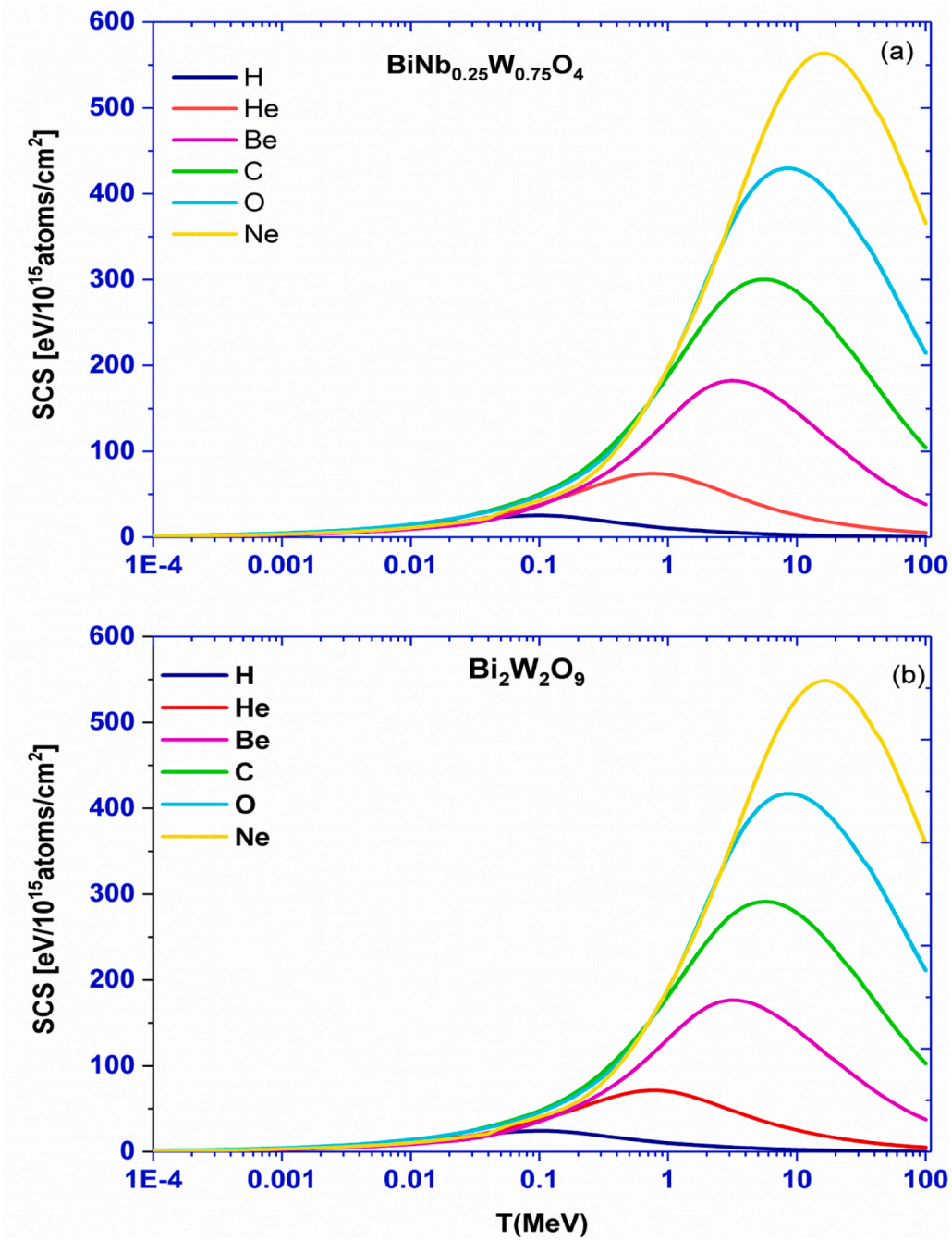

Fig. 8. Electronic SCS of H, He, Be, C, O, and Ne ions on (a) $BiNb_{0.25}W_{0.75}O_4$ and (b) $Bi_2W_2O_9$ based on SRIM simulations.

x = 0.75 and 1, alongside individual elements by Bragg's rule calculations. Heavier ions, such as those with higher atomic mass and atomic number, typically exhibit larger SCSs than lighter ions (e.g., H or He). Heavy ions convey more charge (Ze) and mass (M), resulting in stronger Coulomb interactions with atomic electrons in the $BiNb_{1-x}W_xO_4$ samples. The ion or projectile's initial charge state (q) affects how quickly it loses energy. Fully ionized heavier projectiles tend to have larger electronic SCS than partially ionized lighter projectiles. Consequently, lighter ions interact with matter, influencing their "effective charge state" and, in turn, their electronic energy losses. At kinetic energies ranging from a few keV up to T = 100 MeV, the SCS varies significantly with projectile velocity. In lower energy ranges (<10 MeV), nuclear stopping data (i.e., elastic collisions with atomic nuclei) dominates, whereas at higher energy ranges (>10 MeV), electronic SCS due to ionization and excitation of electrons becomes dominant. Target compositions play a crucial role in evaluating energy loss characteristics, as previously depicted in Fig. 5 and projected ranges in Fig. 6. The presence of heavier elements like Bi, W, and Nb increases the overall electron density distributions, which alters the electronic SCS for all types of projectile ions. Therefore, the compound's stoichiometry may control the amount of energy dissipated during projectile traversal. The changes in energy loss along the ion's trajectory induce an expansion of the PR distribution and multiple Coulomb scattering effects on angular dispersion. The Bragg peak constitutes a semi-sharp maximum in energy particle deposition closer to the end of a projectile's range.

Heavy projectiles generate more noticeable Bragg peaks due to their greater linear energy transfer. In contrast, lighter projectiles like H and He creates broader peaks with smaller noticeable maxima as they deposit less energy per unit path length. Based on Figs. 9**a** and 9**b**, the heavy ions tend to have shorter projected ranges due to higher energy

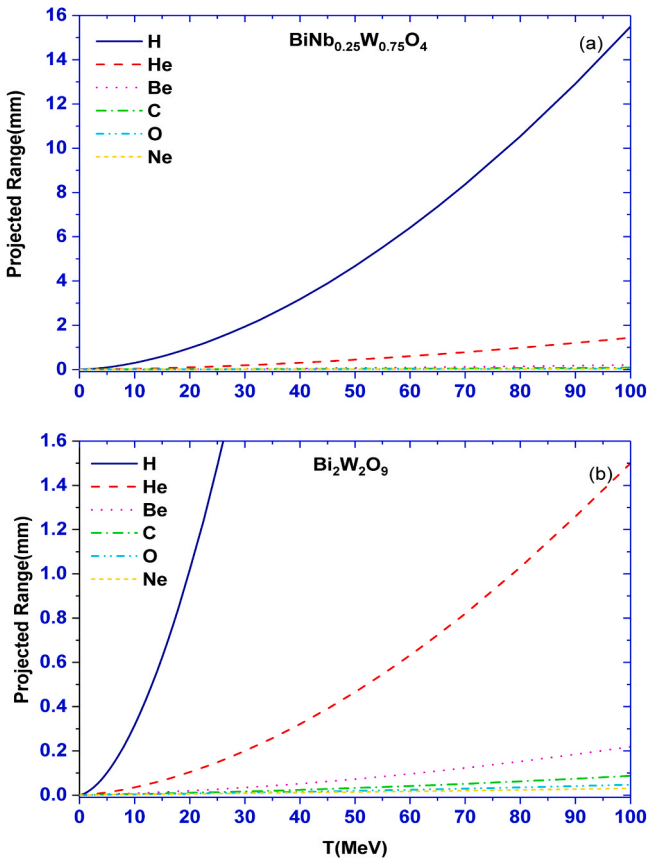

Fig. 9. The PR of H, He, Be, C, O, and Ne ions on (a) $BiNb_{0.25}W_{0.75}O_4$ and (b) $Bi_2W_2O_9$ as determined by SRIM simulations.

loss (see Figs. 8**a** and 8**b**); lighter ions, such as protons, can traverse deeper before losing their kinetic energy. Finally, energy loss and range may be influenced by material composition. In complex dielectric oxides such as $BiNb_{0.25}W_{0.75}O_4$ and $Bi_2W_2O_9$, high-Z elements enhance electronic energy loss efficiency closer to the end of the range region, intensifying or sharpening the Bragg peak for specific ions.

3.7. Proton implantation and damage characterization in $Bi_2W_2O_9$

The complete substitution of a niobium atom with tungsten yields $Bi_2W_2O_9$, as confirmed by the XRD section. The unique properties of $Bi_2W_2O_9$ provide valuable insights for examining radiation damage and proton implantation; its distinct crystal structure can displace and create defects more effectively than other dielectric materials. The implantation was executed within the energy range of 1–10 MeV for H^+ ions in $Bi_2W_2O_9$ using the Sputter Profile Resolution from the Energy Deposition SUSPRE program [63]. The SUSPRE software allows the modeling of a beam of protons with an assigned kinetic energy distribution. The software requires providing ion details, such as name, mass, energy, fluence, angle of incidence, beam current, plot depth, and angle of incidence, in addition to assigning the density and details of the target composition. H^+ ions were implanted with a dose (fluence) of 10^{15} ions/cm^2 and a beam current density of 100 μA/cm^2 to examine the effects of damage and the concentration of protons implanted in $Bi_2W_2O_9$. Developed by Roger Webb at the University of Surrey, the SUSPRE program analyses and simulates the reactions or behavior of ion interactions in dielectrics, including devices and nanomaterials. It is used to ascertain the distribution of implantation ranges for any projectile in single or compound media, so offering an understanding of modeling radiation damage, ion concentration, current distributions, electromagnetic properties, and material performance characteristics. Figs. 10 and 11 represent a 3D

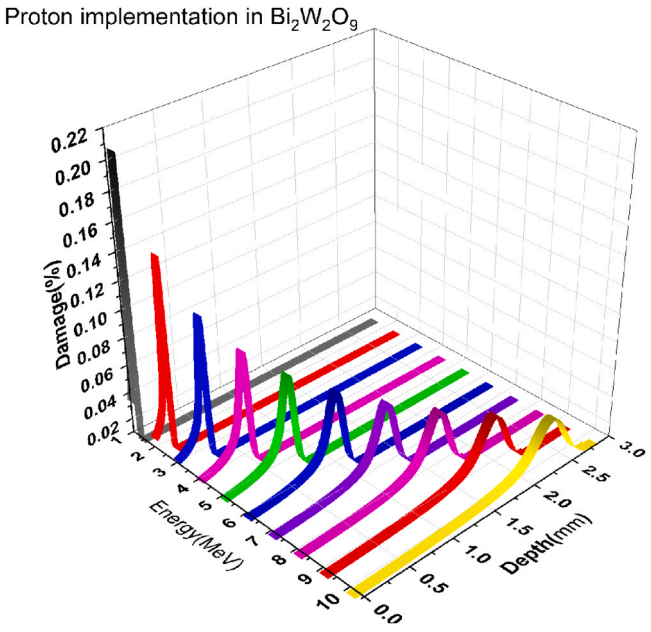

Fig. 10. The predicted damage and ion depth profiles over the energy range of 1–10 MeV for proton implants in $Bi_2W_2O_9$, as computed by SUSPRE [63], with a dose of 10^{15} ions/cm^2, a thickness of 3 mm, and a beam current density of 100 μA/cm^2.

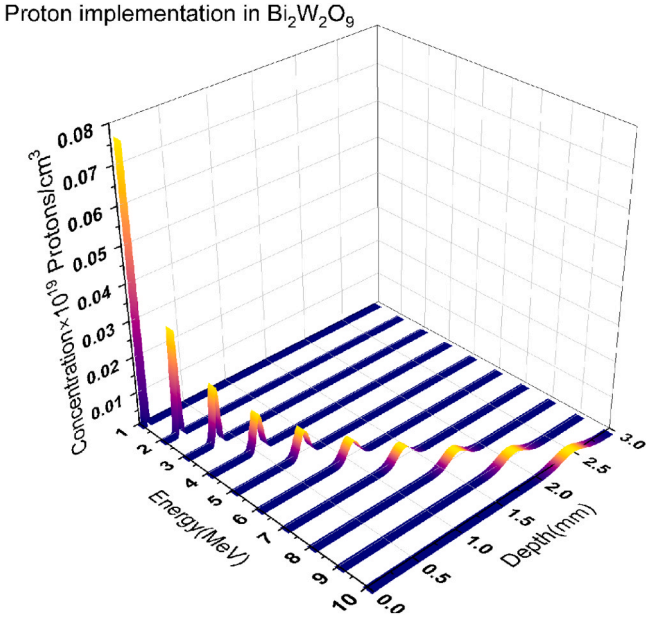

Fig. 11. The predicted concentration and ion depth profiles across the energy range of 1–10 MeV for proton implants in $Bi_2W_2O_9$, as computed by SUSPRE [63], with a dose of 10^{15} ions/cm^2, a thickness of 3 mm, and a beam current density of 100 μA/cm^2.

visualization of the damage and concentration peak profiles for each as a function of proton energies and depth profiles. When a charged beam, such as a proton beam (H^+), is implanted into $Bi_2W_2O_9$, observable effects arise: the stopping of protons is governed by electronic energy loss and nuclear stopping or elastic collisions with nuclei. The depth profile will alter as the projected range of particles increases with beam energy, and the Bragg peak represents maximum energy deposition in matter, penetrating deeper into the compound as energy increases. Displacement damage (damage creation) occurs when protons strike the $Bi_2W_2O_9$

atoms from their lattice sites. The ion concentration follows a normal statistical distribution akin to a Gaussian distribution centered on the projected range. Increasing proton energy causes deeper implantation, reduced surface damage, decreased peak concentration, and a more forward-shifted distributed damage profile. Consequently, the damage per ion decreases with increasing proton energy, but the total damage can remain substantial at higher fluences. The damage caused by proton implantation in $Bi_2W_2O_9$ may lead to several subsequent effects: structural defects such as lattice distortion or swelling due to irradiation with proton energy, amorphization, the creation of oxygen vacancies, and phase transitions. At low proton energy, these consequences are localized at the surface. However, at energies higher than 10 MeV, bulk properties dominate and may potentially modify the electrical and optical characteristics if $Bi_2W_2O_9$ is used in photocatalysts or sensors.

Figs. 12**a** and 12**b** show the simulated concentration and damage distribution of ions as a function of depth profiles of protons implanted in $Bi_2W_2O_9$, using a 5 MeV initial proton beam moving through a 3 mm sample with a current density of 100 μA/cm^2 for different fluence values ranging from 10^{15} to 20×10^{15} ions/cm^2.

After proton penetration in $Bi_2W_2O_9$, it can be observed that the amplitude of the concentration and damage distribution is strongly dependent on the fluence value of the beam, as it increases with a higher fluence. The distribution of the depth profile maintains a Gaussian distribution centered at RP = 0.78 mm. The gradually increasing fluence results in a linear rise in concentration at all depths while the depth shape remains unchanged. Higher implanted doses or fluences correspond to a greater number of implanted protons per mm^3 . The damage

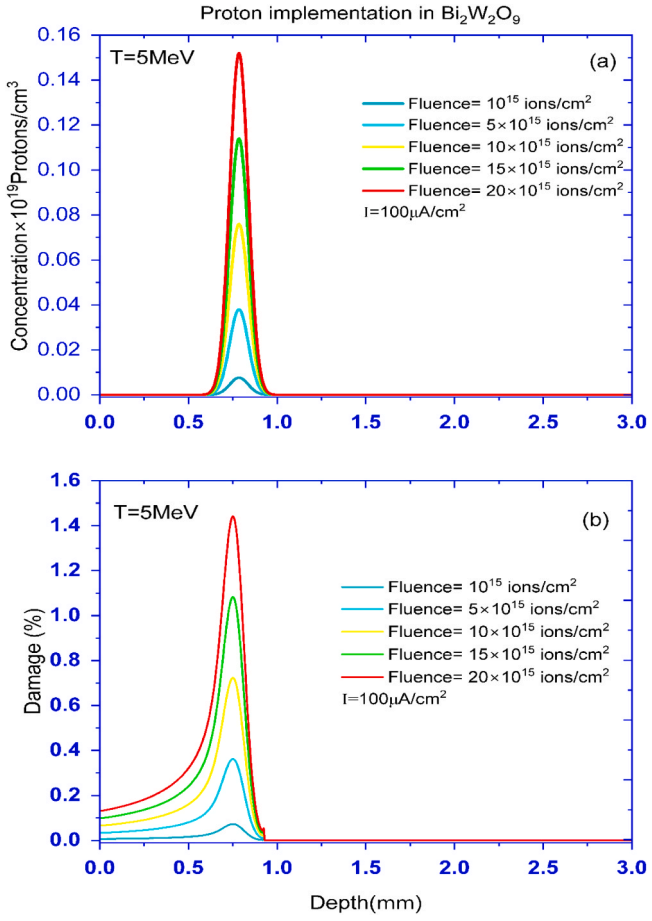

Fig. 12. The SUSPRE simulation of the (a) concentration and (b) damage of protons as a function of the implanted depth profiles in $Bi_2W_2O_9$, utilizing a 5 MeV initial proton beam traveling through 3 mm at a current density of 100 μA/cm^2 in the bismuth tungstate sample for various fluence values.

profile or vacancy production is related to nuclear stopping energy loss interactions. Protons cause atomic displacement damage here, a generally modest but cumulative effect. Particularly when the damage levels reach threshold degrees, the nonlinearly accumulating damage distribution accumulates as doses increase, causing stress-induced swelling or cracking, accumulation of oxygen vacancies, amorphization, and lattice distortion. It should be underlined that changes in the electronic and optical characteristics of $Bi_2W_2O_9$ result from the disturbance of W–O and Bi–O bonds.

3.8. Gamma-ray shielding

The variation of the LAC versus the γ-ray energy was illustrated in Fig. 13**(a-d)**. As shown in Fig. 13**(a)**, when the γ-ray energy increases from 0.015 MeV to 15 MeV, the γ-ray interactions go through three different processes: photoelectric (PE), Compton scattering (CS), and pair production (PP). Across the mentioned PE, CS, and PP interval, the interaction cross-section (σ) for the γ-ray photons changes with $E_\gamma^{-3.5}$, E_γ, and Log E_γ. Under these three various interaction mechanics, the LACs of the fabricated composites varied between 555.185 cm^{-1} and 0.348 cm^{-1} (for the composites with X = 0), 675.539 cm^{-1} and 0.381 cm^{-1} (for the composites with X = 0.25), 797.130 cm^{-1} and 0.415 cm^{-1} (for the composites with X = 0.5), 918.189 cm^{-1} and 0.448 cm^{-1} (for the composites with X = 0.75), and 980.777 cm^{-1} and 0.449 cm^{-1} (for the composites with X = 1), as illustrated in Fig. 13**(a)**. Detailed information about the interaction mechanisms and their dominant energy interval was discussed within the following paragraphs.

The first energy interval extends from 0.015 MeV to 0.122 MeV. The slight increase in the E_γ values results in a significant reduction of the σ values due to the predominance of the photoelectric (PE) interaction. The high reduction in the σ values leads to a high decrease in the number of interactions between γ-photons and the electrons of atoms within the fabricated composites [26,64]. This high decrease in the interaction number is accompanied by a high reduction in the number of photons absorbed within the composite's layer (i.e., I_a photons decreased), while the transmitted photon number increased (i.e., I_t photons increased). This behavior leads to a decrease in the I_o/I_t ratio as the E_γ values increase. This decrease in the (I_o/I_t) ratio give raise to a high decrease in the LACs of fabricated composites as the E_γ increased. Fig. 13 **(b)** shows that the increase in E_γ across the interval of 0.015–0.122 MeV decreases the LACs of fabricated composites with X = 0, X = 0.25, X = 0.5, X = 0.75, and X = 1 across the ranges of 555.185–16.609 cm^{-1}, 675.539–18.623 cm^{-1}, 797.130–21.025 cm^{-1}, 918.189–23.452 cm^{-1}, and 980.777–24.384 cm^{-1}, respectively.

The second energy interval is the CS interaction, which is represented in Fig. 1(c). Across the CS interval, the increase in E_γ values causes a moderate reduction in the σ values. This reduction in σ leads to a decrease a decrease in (I_a) photons and an increase in the (I_t) photons. The (I_o/I_t) ratio suffers a decrease, which leads to a reduction in the LACs of fabricated composites. The reduction in the LACs across the CS interval is moderate compared to the reduction in the LACs which was achieved at PE interactions. Fig. 13 **(c)** reveals that the increase in E_γ from 0.122 to 1.022 MeV is followed by a moderate reduction in the LACs of composites with X = 0, X = 0.25, X = 0.5, X = 0.75, and X = 1 across the intervals of 16.609–0.486 cm^{-1}, 18.623–0.536 cm^{-1}, 21.025–0.569 cm^{-1}, 23.452–0.605 cm^{-1}, αvδ 24.384–0.575 cm^{-1}.

The third energy interval is the PP interaction, which extends over the energy range varied between 1.022 MeV and 15 MeV, as illustrated in Fig. 13 **(d)**. The PP interaction starts within the fabricated composites at 1.022 MeV, but it is not high enough compared to the CS interaction. The CS is still the dominant interaction up to E_γ of 5 MeV. Therefore, the increase in the E_γ from 1.022 MeV to 5 MeV is accompanied by a reduction in the LACs throughout the ranges of 0.486–0.289 cm^{-1} (for the composite with X = 0), 0.536–0.312 cm^{-1} (for the composite with

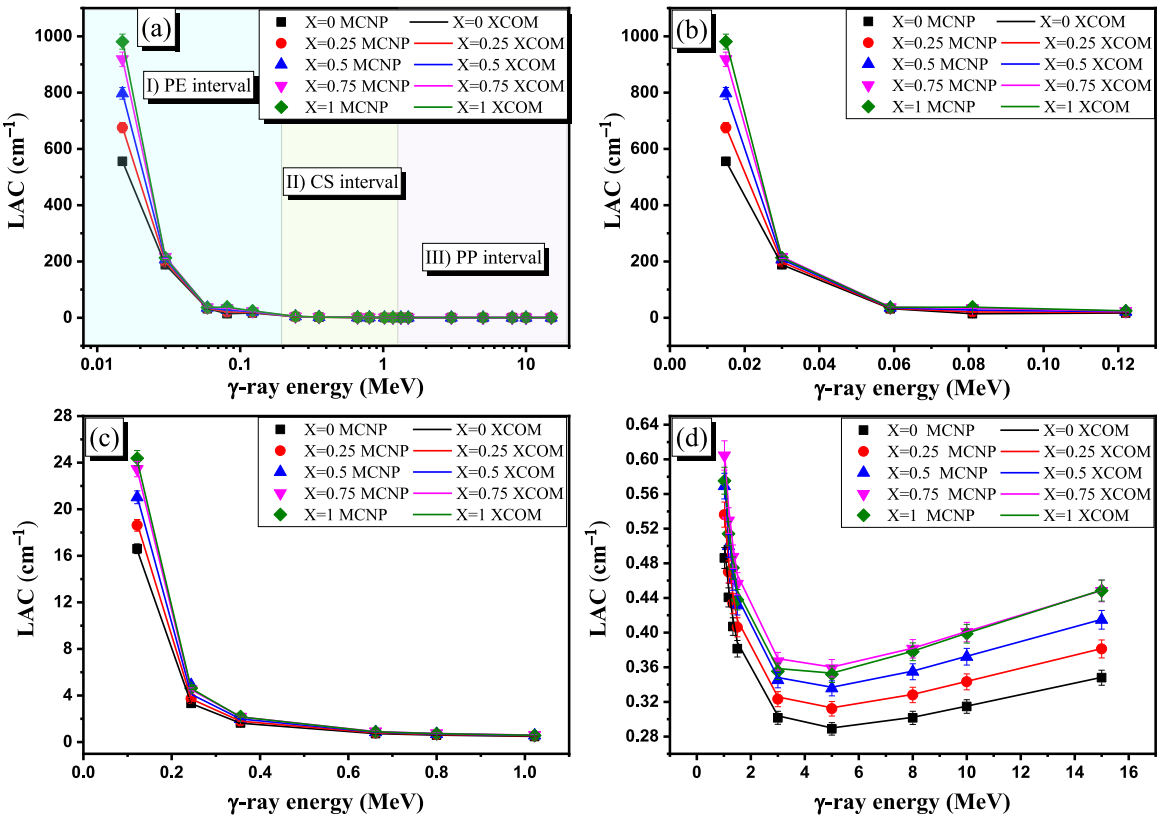

Fig. 13. The impact of the γ-ray energy on (a) total linear attenuation coefficient, (b) linear attenuation coefficient at PE interval, (c) linear attenuation coefficient at CS interval, and (d) linear attenuation coefficient at PP interval.

X = 0.25), 0.569–0.336 cm^{-1} (for the composite with X = 0.5), 0.605–0.359 cm^{-1} (for the composite with X = 0.75), and 0.575–0.352 cm^{-1} (for the composite with X = 1). Above 5 MeV, a slight increase in the LACs is observed due to the slight increase in σ values following the high raises in the E_γ. This behavior is a confirmation for the prevalent of PP interaction at E_γ interval above 5 MeV. According to the data presented in Fig. 13 **(d)**, the increase in E_γ from 5 MeV to 15 MeV is accompanied by a tiny increase in the LACs across ranges of 0.289–0.348 cm^{-1} (for the composite with X = 0), 0.312–0.381 cm^{-1} (for the composite with X = 0.25), 0.336–0.415 cm^{-1} (for the composite with X = 0.5), 0.359–0.448 cm^{-1} (for the composite with X = 0.75), and 0.352–0.449 cm^{-1} (for the composite with X = 1). Fig. 13 **(a-d)** show an agreement between the simulated LACs and the LACs, which are calculated based on the calculation performed using the XCOM program. The difference between both methods ranging ±3%.

To validate the shielding efficiency of the fabricated $BiNb_{1-x}WxO_4$ composites, their LACs were compared to some commercial protective lead-based glasses supplied by Schott AG [1], pure PbO, and Bi_2O_3 composites, as presented in Fig. 14. The LACs of the fabricated $BiNb_{1-x}WxO_4$ composites at 0.662 MeV are 0.728 cm^{-1}, 0.792 cm^{-1}, 0.853 cm^{-1}, 0.924 cm^{-1}, and 0.896 cm^{-1} for composites with X = 0, X = 0.25, X = 0.75, and X = 1, respectively. These LAC values for the $BiNb_{1-x}W_xO_4$ composites are high compared to the LACs of lead-based protective glasses RS 253 (0.19 cm^{-1}), RS 253 G18 (0.19 cm^{-1}), RS 323 G19 (0.28 cm^{-1}), RS 360 (0.32 cm^{-1}), and RS 520 (0.5 cm^{-1}). The high LACs for the $BiNb_{1-x}W_xO_4$ composites are attributed to their high content of heavy metals Bi, W, and Nb. On the other hand, the LACs of fabricated BiNb1 $-xW_xO_4$ composites are lower than the LAC of pure PbO (1.0273 cm^{-1}). Additionally, the fabricated $BiNb_{1-x}W_xO_4$ composites, especially for composites with X = 0.75 and X = 1, are slightly lower than the LAC of pure Bi_2O_3 (0.969 cm^{-1}). These results show the potential effect of the prepared composites in the radiation shielding applications.

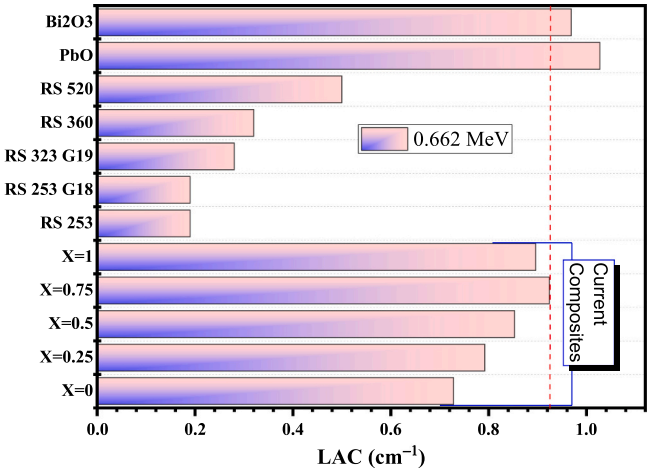

Fig. 14. Comparing the linear attenuation coefficient of the prepared $BiNb_{1-x}W_xO_4$ composites with the commercial radiation protective glasses.

Additionally, the HVLs for the prepared $BiNb_{1-x}W_xO_4$ composites have a variation that tends opposite to that illustrated early for the LACs. The reason for this behavior is the reverse variation of the HVLs and LACs. The thinner HVLs were observed at the low energy interval (i.e., PE interval). These thinner values were between 0.001 and 0.042 cm for the composite with X = 0, 0.001 and 0.037 cm for the composite with X = 0.25, 0.001 and 0.033 cm for the composite with X = 0.5, 0.001 and 0.030 cm for the composite with X = 0.75, and 0.001 and 0.028 cm for the composite with X = 1, as the photon energy went up from 0.015 MeV to 0.122 MeV, as shown in Fig. 15. Thereafter, with increasing the CS interaction inside the fabricated composites, the (I_t)

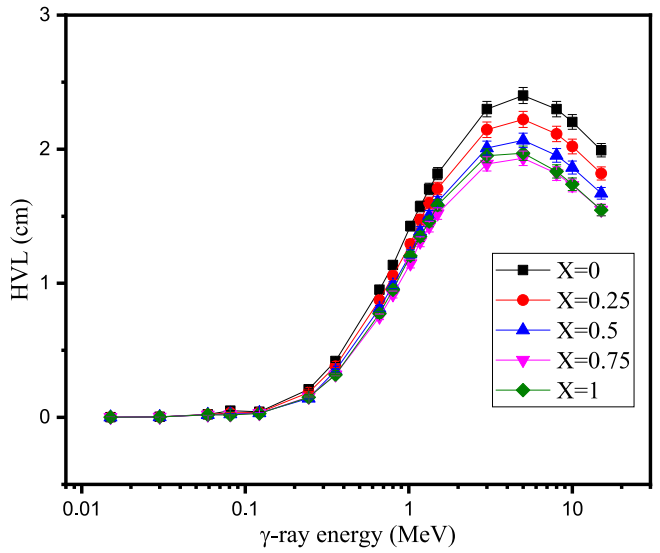

Fig. 15. The impact of γ-ray energy on the half value-layer (HVL, cm) of the prepared $BiNb_{1-x}W_xO_4$ composites.

photons strongly increased, which gave rise to a strong increase in the thickness required to reduce it to 50% of Io values. Fig. 15 reveals that the increase in E_γ from 0.122 MeV to 1.022 MeV is accompanied by a high increase in the HVLs from 0.042 to 1.426 cm (for the composite with X = 0), 0.037–1.293 cm (for the composite with X = 2.5), 0.033–1.218 cm (for the composite with X = 0.5), 0.030–1.147 cm (for the composite with X = 0.75), and 0.028–1.205 cm (for the composite with X = 1), respectively. The HVL increased slightly with raising the E_γ values over the interval of photons, which varied between 1.022 MeV and 5 MeV, due to the reduction of the σ values over the CS interval. After that, above 5 MeV, the increase in E_γ values is accompanied by a small reduction in the HVLs due to the PP interaction. The data in Fig. 15 shows that when E_γ increases from 5 MeV to 15 MeV, the HVLs of the composites with X = 0, X = 0.25, X = 0.5, X = 0.75, and X = 1 decrease across the ranges of 2.400–1.992 cm, 2.222–1.819 cm, 2.066–1.671 cm, 1.932–1.547 cm, and 1.970–1.545 cm, respectively.

It is known that a thickness of 0.05 cm of lead-equivalent materials is required for protection in medical applications. In the current section, the thickness equivalent to 0.05 cm of pure lead (TEL, cm) was calculated for the prepared $BiNb_{1-x}W_xO_4$ composites at various γ-ray energies, as illustrated in Fig. 16. At the PE interaction, the TELs for the fabricated composites don't have any identified trend and fluctuated throughout the intervals of 0.113–0.094 cm, 0.093–0.065 cm, 0.079–0.048 cm, 0.069–0.039 cm, and 0.064–0.035 cm for $BiNb1-xWxO_4$ composites when X = 0, X = 0.25, X = 0.5, X = 0.75, and X = 1, respectively, when the Eγ increased from 0.015 MeV to 0.081 MeV. These fluctuations are attributed to the K-absorption edges of Bi, W, and Nb that appear at the mentioned interval [27]. Near 0.122 MeV, the TELs increase to higher intervals due to the K-absorption of Pb, which causes the LACs of Pb to compare to the fabricated composites around the mentioned energies. Thereafter, the increase in the Eγ values from 0.122 MeV to 1.022 MeV is accompanied by a reduction in the TELs throughout the intervals of 0.114–0.081 cm, 0.102–0.073 cm, 0.090–0.069 cm, 0.081–0.065 cm, 0.078 cm, and 0.068 cm, respectively, for the fabricated composites with X = 0, X = 0.25, X = 0.5, X = 0.75, and X = 1. The exponential reduction in the TLS is attributed to the comparable reduction in LACs of pure Pb and fabricated composites. The increase in the photon's energy from 0.122 MeV to 1.022 MeV is accompanied by an exponential reduction in the LAC of Pb and fabricated composites by ≈ 97%. Over the interval that extends from 1.022 MeV to 3 MeV, the TELs still decrease with raising the γ-ray energy due to the predominance of CS interaction, as illustrated in the early sections. Above 3 MeV, the TELs began to increase in both LACs of Pb and fabricated composites. The increase in the Eγ from 3 to 15 MeV causes a small raise in the TELs across the ranges of 0.079–0.092 cm (for the composite with X = 0), 0.074–0.084 cm (for the composite with X = 0.25), 0.069–0.077 cm (for the composite with X = 0.5), 0.065–0.071 cm (for the composite with X = 0.75), and 0.067–0.071 cm (for the composite with X = 1), respectively.

The RPE for the prepared $BiNb_{1-x}W_xO_4$ composites are significantly affected by the mechanism of γ-ray interaction, as illustrated in Fig. 17. At the PE interval, the photon energies are small, and they are totally consumed during the interaction with electrons inside the atoms consisting of the fabricated composites. Therefore, the (I_a) photons reach their maximum values at the PE interval, which is the main reason for the maximum RPEs (i.e., 100% for all samples) obtained for the prepared composites over the interval varied between 0.015 and 0.122 MeV. Then, due to the increase in CS interaction with raising the photon energy above 0.122 MeV, the number of scattered and transmitted photons (I_t) increased while the absorbed photons (I_a) reduced. This decline in the I_a photon causes a reduction in the I_a/I_o ratio and RPEs. According to Fig. 17, the increase in γ-ray energy from 0.122 MeV to 1.022 MeV decreases the RPEs of fabricated $BiNb_{1-x}W_xO_4$ composites

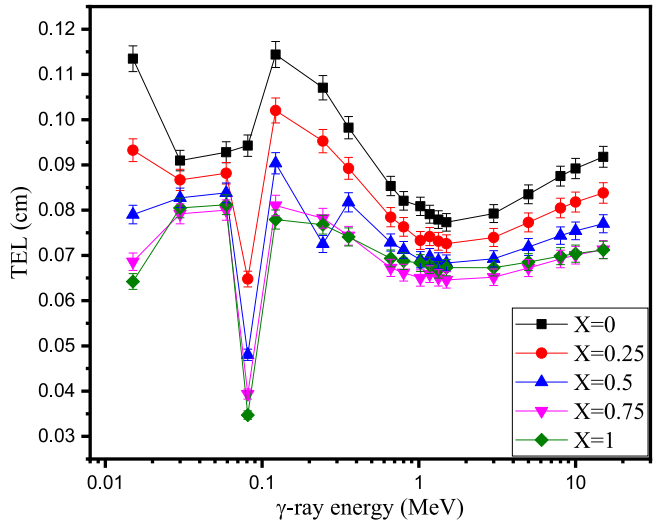

Fig. 16. The influence of γ-ray energy on the thickness equivalent lead (TEL, cm) of the prepared $BiNb_{1-x}W_xO_4$ composites.

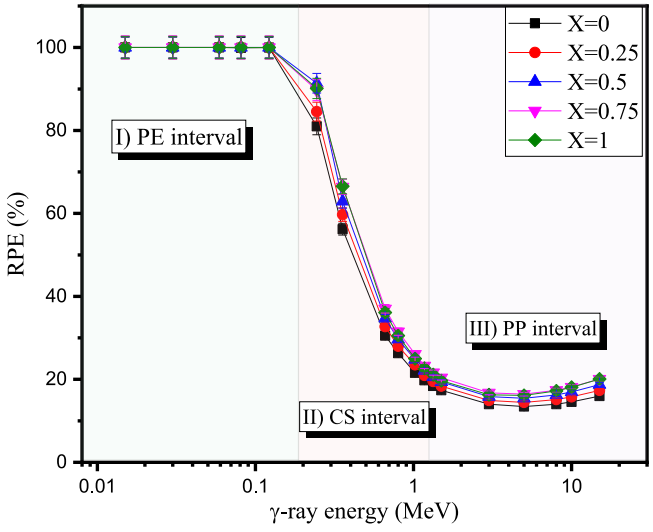

Fig. 17. The radiation protection efficiency (RPE, %) of $BiNb_{1-x}W_xO_4$ composites at various γ-ray energies (i.e., across the PE, CS, and PP intervals).

with X = 0, X = 0.25, X = 0.5, X = 0.75, and X = 1 across the ranges of 99.98–21.58%, 99.99–23.52%, 100.00–24.77%, 100.00–26.09%, and 100.00–25.00%, respectively. Then across the PP interval, due to the slight increase in the σ values, the interactions between the incident γ-rays and electrons in the fabricated composites increased. Therefore, the (I_a) photons start a slight increase, which leads to a slight increase in the RPEs of prepared composites. The increase in E_γ from 5 MeV to 15 MeV causes a slight increase in the RPEs across the ranges of 13.45–15.97% for the composite with X = 0, 14.44–17.35% for the composite with X = 0.25, 15.45–18.73% for the composite with X = 0.5, 16.42–20.07% for the composite with X = 0.75, and 16.13–20.09% for the composite with X = 1. The substitution of W for the Nb contents has great impacts on the density (ρ, g/cm^3) and effective atomic number (Z_{eff}) of the prepared composites. Due to the high density of W (19.254 g/cm^3) compared to Nb (8.582 g/cm^3), the substitution of W for the Nb atoms increases the density of the prepared composites. According to Fig. 18, the increase in W content from 0 to 41.71 wt% increases the ρ values of fabricated composites from 7.58 g/cm^3 to 8.7 g/cm^3. This increase in the prepared ρ values of the fabricated composites is attributed to the increase in Z_{eff} of prepared composites when the W substituted the Nb contents. The calculations indicate that the increase in W content within the prepared composites from 0 to 41.71 wt% increases the Z_{eff} values from 69.89 to 76.00, respectively.

Raising the W content leads to higher ρ and Z_{eff} values, which improves the shielding properties of the fabricated samples. These enhancements are related to the variation of the σ values with $Z_{eff}^{4.6}$, Z_{eff}, and Z_{eff}^{2} over the PE, CS, and PP interaction intervals. Therefore, the increase in W content is accompanied by a high enhancement in the shielding properties at the PE interval compared to the enhancements achieved at the CS and PP intervals. Fig. 19 reveals that the increase in the W content from 0 to 41.71 wt% is accompanied by an increase in the LACs from 31.877 cm^{-1} to 36.433 cm^{-1} at 0.059 MeV, 0.728 cm^{-1} to 0.896 cm^{-1} at 0.662 MeV, and 0.315 cm^{-1} to 0.399 cm^{-1} at 10 MeV.

The increase in the LACs of the fabricated composites leads to a decrease in the HVLs of the prepared composites, as shown in Fig. 20. The main reason for the reduction in LACs is the inverse relationship between the LACs and HVLs as the W content increases. The data in Fig. 20 show that increasing the W concentration from 0 to 41.71 wt% lowers the HVLs to 0.019 cm (at 0.059 MeV), 0.773 cm (at 0.662 MeV), and 1.738 cm (at 10 MeV).

Additionally, raising the W concentration within the fabricated composites increases the LACs of fabricated composites compared to the LACs of pure Pb. Therefore, Fig. 21 reveals a decrease in the TELs as the W content increased within the fabricated composites. According to

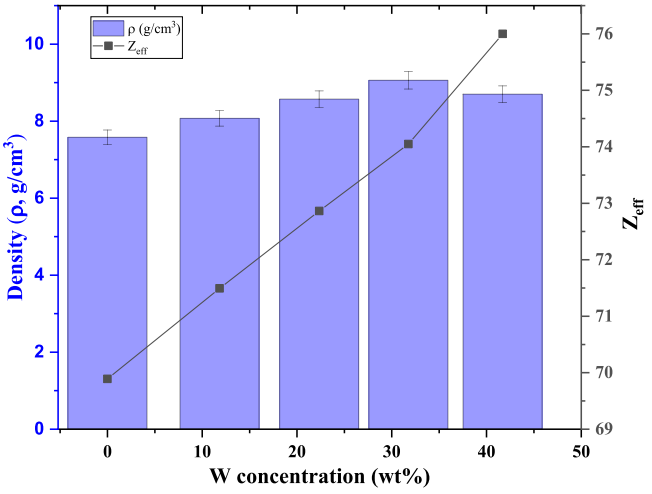

Fig. 18. The influence of raising the W concentrations on the density (ρ, g/cm^3) and effective atomic number (Z_{eff}) of prepared $BiNb_{1-x}W_xO_4$ composites.

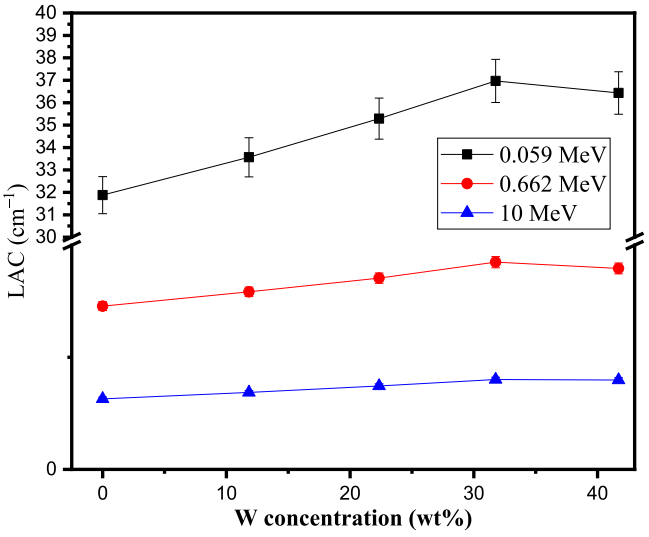

Fig. 19. The effect of W concentrations on the linear attenuation coefficient (LAC, cm^{-1}) of $BiNb_{1-x}W_xO_4$ composites.

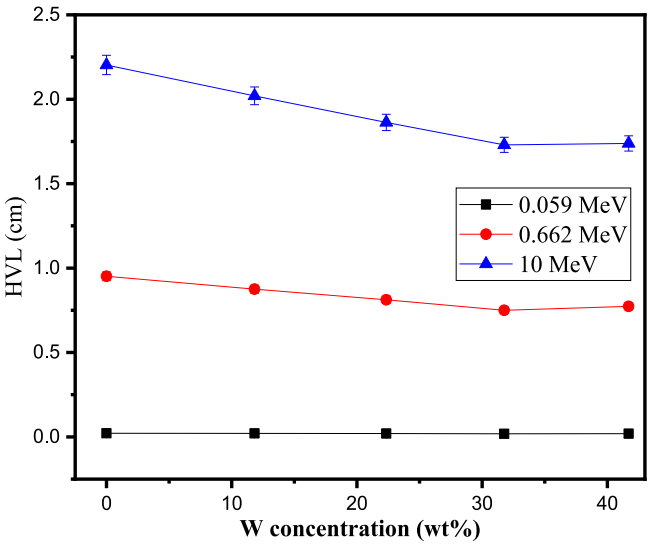

Fig. 20. The effect of W concentrations on the half-values layer (HVL, cm) of $BiNb_{1-x}W_xO_4$ composites.

Fig. 21, increasing the W content from 0 to 41.71 wt% reduces the TELs of the $BiNb_{1-x}W_xO_4$ composites in the ranges of 0.093–0.081 cm (at 0.059 MeV), 0.085–0.069 cm (at 0.662 MeV), and 0.089–0.070 cm (at 10 MeV).

As previously illustrated, the increase in W content increases the σ, which increases photon interaction probability with the electron in the fabricated materials. Therefore, the absorbed photons (I_a) increased, leading to an increase in the I_a/I_o ratio and RPE as the W content increases. Fig. 22 reveals an increase in the RPEs of 0.5 cm thickness of the fabricated composites from 30.52% to 36.12% (at 0.662 MeV) and 14.56–18.07% (at 10 MeV) when the W content raised from 0 wt% to 41.71 wt%, respectively. Furthermore, for all energies ≤ 0.122 MeV, including 0.059 MeV, the RPEs are close to 100% due to the PE interaction.

4. Conclusion

The present study evaluates $BiNb_{1-x}W_xO_4$ as a structurally adaptable, composition variable system, allowing for smooth changes in its crystal

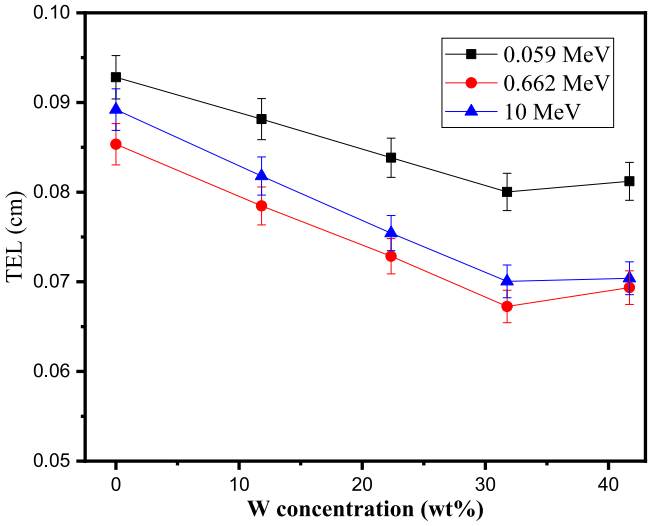

Fig. 21. The variation of the thickness equivalent lead (TEL, cm) for the $BiNb_{1-x}W_xO_4$ composites at various W concentrations.

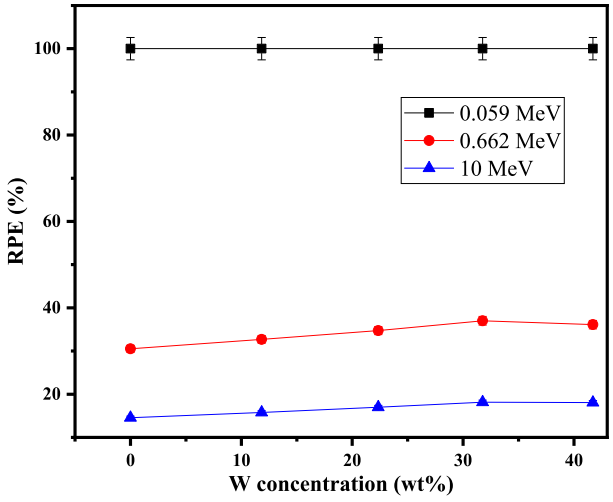

Fig. 22. The variation of the radiation protection efficiency (RPE, %) of $BiNb_{1-x}W_xO_4$ composites at various W concentrations.

chemistry from the orthorhombic α-$BiNbO_4$ lattice to the tungstate-like structure of orthorhombic γ-Bi_2WO_6, without the formation of secondary phases. The systematic peak changes in XRD and the development of Nb-O/W-O vibrational signatures validate authentic solid-solution formation, demonstrating that tungsten substitution gradually bends the BO_6 polyhedron, serving as an atomistic mechanism for manipulating local bonding and, ultimately, bulk functionality. Simultaneously, all compositions maintain nanometric dimensions, with a minimum particle size around x = 0.5, indicative of the conflicting effects of lattice strain and diffusion-controlled development. As x goes from 0 to 0.75, the predicted density goes up from 7.5 to 9.5 g cm^{-3} . This means that γ- and X-ray attenuation gets stronger, putting the W-rich end members in a position to compete with or even beat traditional lead shields while getting rid of the dangers of heavy metals. Simulations of ion transport offer more evidence of its radiological significance. Using the SRIM code, we can see that both the proton stopping cross-section and projected range contraction decrease steadily as the W content increases, reaching their lowest points at x = 0.75. These trends are very similar to the experimental values stored in the IAEA stopping-power database and follow Bragg's additivity rule, which shows that the predictions are reliable. Also, SUSPRE modeling shows that 5 MeV protons are halted inside the last 0.78 mm of dense $Bi_2W_2O_9$, which confirms a steep energy-loss gradient that is good for targeted beam stopping and ion-beam patterning. These insights into the structure, microstructure, and ion interactions all point to W-rich $BiNb_{1-x}W_xO_4$ as an environmentally friendly, strong, lead-free shield for both photon and charged-particle environments. The subsequent investigation must focus on the sintering of these nanoscale powders into fully dense entities, assess their long-term radiation resistance and thermomechanical stability, and empirically validate the anticipated stopping capability throughout a broader spectrum of energetic particles. The goal of these initiatives is to make it clearer what this flexible oxide family can do in nuclear facilities, medical imaging suites, and electronics that work in space. The Monte Carlo tests show that the $BiNb_{1-x}W_xO_4$ composites that were made are better at blocking radiation than commercial lead-based protective eyewear. The prepared composites have the highest linear attenuation coefficient of 0.92 cm^{-1} at a γ-ray energy of 0.662 MeV. This is when x = 0.75 (i.e., the $BiNb_{0.25}W_{0.75}O_4$ composite). This is 1.84 times higher than the commercial radiation protective glass RS 520, which is made up of 71 wt% PbO. Thus, hospitals can employ the produced composites instead of lead-based materials for protection in diagnostic and nuclear treatment settings. It can also be used to defend against strong gamma-ray energy in nuclear reactors.

CRediT authorship contribution statement

Usama Altimari: Writing – review & editing, Writing – original draft. **Kawa M. Kaky:** Writing – review & editing, Writing – original draft. **M.H.A. Mhareb:** Writing – review & editing, Writing – original draft, Methodology, Investigation. **Sayyed M.I.:** Writing – review & editing, Writing – original draft, Supervision, Methodology. **Nabil Janan Al-Bahnam:** Writing – review & editing, Writing – original draft, Software, Methodology. **Mahmoud K. A.:** Writing – review & editing, Writing – original draft, Data curation, Conceptualization. **Rahman I. Mahdi:** Writing – review & editing, Writing – original draft, Methodology, Investigation.

Declaration of Competing Interest

Kawa M. Kaky If there are other authors, they declare that they have no known competing financial interests or personal relationships that could have appeared to influence the work reported in this paper.

Data availability

Data will be made available on request.

References

[1] S.M. Kassem, et al., Novel flexible and lead-free gamma radiation shielding nanocomposites based on LDPE/SBR blend and BaWO4/B2O3 heterostructures, Radiat. Phys. Chem. 209 (2023) 110953.
[2] C.V. Vishnu, A. Joseph, Gamma-ray shielding analysis on natural rubber composites fortified with barium tungstate (BaWO4), Radiat. Phys. Chem. 216 (2024) 111389.
[3] M.I. Sayyed, et al., Recycling and optimizing waste lab glass with Bi2O3 nanoparticles to use as a transparent shield for photons, J. Mater. Res. Technol. 17 (2022) 2073–2083.
[4] M.A. Ajeel, et al., Preparation and characterization of electrode from annealed nano-diamond particles with boric acid for anodic oxidation process, Electrochim. Acta 362 (2020) 137221.
[5] R.I. Mahdi, et al., Enhanced visible-light degradation of cationic dyes over BiTaO4/BiVO4 heterostructure nanoplates, Materials Science Engineering B 323 (2026) 118699.
[6] R. Mahdi, et al., Photocatalytic Hydrogen Generation from pH-Neutral Water by a Flexible Tri-Component Composite, Catal. Lett. 151 (6) (2021) 1700–1706.
[7] R. Mahdi, et al., Photocatalytic hydrogen generation from ph-neutral water by a flexible Tri-component composite, Catal. Lett. (2020).
[8] A. Al-Keisy, et al., Enhanced photoreduction activity in BiOI1-xFx nanosheet for efficient removal of pollutants from aqueous solution, ChemistrySelect 5 (31) (2020) 9758–9764.

[9] R.I. Mahdi, et al., Optimization of sintering temperature for the enhancement of pyroelectric properties of lead-free 0.88(Na0.5Bi0.5)TiO3–0.084(K0.5Bi0.5)TiO3–0.036BaTiO3 piezoelectric ceramics, J. Alloy. Compd. 688 (2016) 77–87.

[10] M.Z. Hossain, et al., Combined experimental and DFT approach to BiNbO4 polymorphs, RSC Adv. 13 (8) (2023) 5576–5589.

[11] W. Liu, M. Xu, M. Zhu, Design of a niobium tungsten oxide/C micro-structured electrode for fast charging lithium-ion batteries, Inorg. Chem. Front. 8 (17) (2021) 3998–4005.

[12] Z. Li, et al., Nanofilms based on superstructured niobium tungsten oxide have high dual-functional potential for electrochromism and energy storage, Appl. Surf. Sci. 666 (2024) 160394.

[13] F. Krok, et al., Effects of low levels of tungsten doping in bismuth niobates, Solid State Ion. 179 (1) (2008) 172–177.

[14] A. Elaouni, et al., Bismuth tungstate Bi2WO6: a review on structural, photophysical and photocatalytic properties, RSC Adv. 13 (26) (2023) 17476–17494.

[15] M.M. Najm, et al., Performance investigation and optimization of EDFL based on Lithium Niobate–Titanium Oxide nanomaterial saturable absorber, Opt. Mater. 165 (2025) 117118.

[16] R.I. Mahdi, et al., Nanostructured LNTO saturable absorber for generating multi-wavelength laser in Q-switched EDFL, Opt. Mater. 157 (2024) 116122.

[17] C.-M. Cheng, S.-H. Lo, C.-F. Yang, The effect of CuO on the sintering and properties of BiNbO4 microwave ceramics, Ceram. Int. 26 (1) (2000) 113–117.

[18] R. Mahdi, et al., Tailoring the morphology of BiNbO4 of polymorph in 2D nanosheets for enhancement of photocatalytic activity in the visible range, Phys. E Lowdimensional Syst. Nanostruct. 136 (2022) 115009.

[19] S. Devesa, M.P. Graça, L.C. Costa, Structural, morphological and dielectric properties of BiNbO4 ceramics prepared by the sol-gel method, Mater. Res. Bull. 78 (2016) 128–133.

[20] N. Wang, et al., Effects of complex substitution of La and Nd for Bi on the microwave dielectric properties of BiNbO4 ceramics, Mater. Res. Bull. 39 (3) (2004) 439–448.

[21] R.I. Mahdi, et al., Engineered composition and morphology: Unveiling 2D $Bi_2(W_{1-x}Mox)O_6$ nanosheets for enhanced optical and ionizing protection applications, Mater. Today Commun. 45 (2025) 112415.

[22] M.A. Subramanian, J.C. Calabrese, Crystal structure of the low temperature form of bismuth niobium oxide [α-BiNbO4, Mater. Res. Bull. 28 (6) (1993) 523–529.

[23] N.A. Zhuk, et al., High-Temperature Crystal Chemistry of α-, β-, and γ-BiNbO4 Polymorphs, Inorg. Chem. 58 (2) (2019) 1518–1526.

[24] E. Hannachi, et al., Scheelite-type BaWO4 doped with Ho2O3 oxide as a promising lead-free shield for gamma rays: structural, optical properties, and radiation attenuation efficiency, Mater. Sci. Semicond. Process. 167 (2023) 107802.

[25] M. Yılmaz, F. Akman, Gamma radiation shielding properties for polymer composites reinforced with bismuth tungstate in different proportions, Appl. Radiat. Isot. 200 (2023) 110994.

[26] M.H.A. Mhareb, et al., Role of Nd (III) ions on B2O3–TeO2-GeO2-MgO glass composition for optical and ionizing protection application, Nucl. Eng. Technol. 57 (1) (2025) 103162.

[27] K.M. Kaky, et al., Comprehensive investigations of niobium pentoxide effects on B2O3–TeO2-GeO2-MgO glass system for optical and radiation absorption applications, Radiat. Phys. Chem. 232 (2025) 112612.

[28] M.I. Sayyed, et al., Design, fabrication, and features investigations of high concentration of Yttrium Oxide doped germanate tellurate borate glass system for optical and radiation shielding application, Ceram. Int. 50 (24, Part B) (2024) 54490–54497.

[29] M.I. Sayyed, et al., Optical, physical, mechanical, structural, and radiation shielding investigations of B2O3–TeO2-GeO2-MgO-PbO for ionizing protection and optical transmission application, Opt. Mater. 154 (2024) 115807.

[30] MCNP, X., *Monte carlo team, mcnp–a general purpose monte carlo n-particle transport code, version 5*. 2003, LA-UR-03-1987, Los Alamos National Laboratory.

[31] J.-C. Champarnaud-Mesjard, B. Frit, A. Watanabe, Crystal structure of Bi2W2O9, the n=2 member of the homologous series (Bi2O2)BVIO3n+1 of cation-deficient Aurivillius phases, J. Mater. Chem. 9 (6) (1999) 1319–1322.

[32] G. George, et al., Rare-earth-doped electrospun scheelite CaWO4 nanofibers with excitation-dependent photoluminescence and high-linearity cathodoluminescence for ratiometric UV wavelength and radiation sensors, Opt. Mater. 126 (2022) 112130.

[33] B. Wang, et al., A comparative study between pure bismuth/tungsten and the bismuth tungsten oxide for flexible shielding of gamma/X rays, Radiat. Phys. Chem. 208 (2023) 110906.

[34] D. Errandonea, F.J. Manjón, Pressure effects on the structural and electronic properties of ABX4 scintillating crystals, Prog. Mater. Sci. 53 (4) (2008) 711–773.

[35] J.-C. Champarnaud-Mesjard, B. Frit, A. Watanabe, Crystal structure of Bi 2 W 2 O 9, the n= 2 member of the homologous series (Bi 2 O 2) B VI n O 3n+ 1 of cation-deficient Aurivillius phases, J. Mater. Chem. 9 (6) (1999) 1319–1322.

[36] R. Ullah, et al., Synthesis of doped BiNbO4 photocatalysts for removal of gaseous volatile organic compounds with artificial sunlight, Chem. Eng. J. 185-186 (2012) 328–336.

[37] M. Imtiaz, et al., Bismuth niobium oxide (BiNbO4) coated on rGO nanocomposite formation for the application of the supercapacitor, Materials Science Engineering B 313 (2025) 117919.

[38] A. Meera, et al., The significant role of Z-scheme band alignment at the heterojunction for the enhanced photocatalytic H2 production in TiO2/BiNbO4/rGO nanocomposite, J. Solid State Chem. 340 (2024) 125030.

[39] M. Mączka, L. Macalik, J. Hanuza, Raman and IR spectra of the cation-deficient Aurivillius layered crystal Bi2W2O9, J. Raman Spectrosc. 40 (12) (2009) 2099–2103.

[40] L. Xu, et al., Crystal structure evolution, bond characteristics and tunable microwave dielectric properties of (Ce1-xCax)(Nb1-xWx)O4 ceramics, J. Eur. Ceram. Soc. 44 (7) (2024) 4657–4665.

[41] K. Nakamoto, Infrared and Raman Spectra of Inorganic and Coordination Compounds, Handb. Vib. Spectrosc. (2001).

[42] J.F. Ziegler, M.D. Ziegler, J.P. Biersack, SRIM – The stopping and range of ions in matter (2010), Nucl. Instrum. Methods Phys. Res. Sect. B Beam Interact. Mater. At. 268 (11) (2010) 1818–1823.

[43] Z. Vager, D.S. Gemmell, Polarization Induced in a Solid by the Passage of Fast Charged Particles, Phys. Rev. Lett. 37 (20) (1976) 1352–1354.

[44] G. Schiwietz, et al., Femtosecond dynamics – snapshots of the early ion-track evolution, Nucl. Instrum. Methods Phys. Res. Sect. B Beam Interact. Mater. At. 226 (4) (2004) 683–704.

[45] N.J. Al-Bahnam, R.I. Mahdi, A.I.A. Al-Numan, The Induced Electron Density Effects of Swift Heavy Ions in Polymethyl Methacrylate, Braz. J. Phys. 49 (1) (2019) 1–9.

[46] A. Schinner, P. Sigmund, Polarization wake of penetrating ions: oscillator model, Eur. J. Phys. 66 (2) (2012) 1–11.

[47] A.S. Naje, et al., Enhancement of ionic mass transfer coefficient using a unique electrocoagulation reactor with rotating impeller anode, Sep. Sci. Technol. 55 (6) (2020) 1167–1176.

[48] N.J. Al-Bahnam, et al., Describing the differential inelastic inverse mean free path of PMMA polymer with the Mermin–Belkacem-Sigmund model, Indian J. Phys. 97 (9) (2023) 2599–2610.

[49] W. Chaiphaksa, et al., Computational approach of alpha and proton interaction of gadolinium bismuth borate glass system using SRIM program, Mater. Today. Proc. 65 (2022) 2416–2420.

[50] J.E. Valdés, et al., Electronic energy loss of low velocity H+ beams in Al, Ag, Sb, Au and Bi, Nucl. Instrum. Methods Phys. Res. Sect. B Beam Interact. Mater. At. 73 (3) (1993) 313–318.

[51] M.V. Moro, P. Bauer, D. Primetzhofer, Experimental electronic stopping cross section of transition metals for light ions: Systematics around the stopping maximum, Phys. Rev. A 102 (2) (2020) 022808.

[52] M.V. Moro, et al., Experimental electronic stopping cross section of tungsten for light ions in a large energy interval, Nucl. Instrum. Methods Phys. Res. Sect. B Beam Interact. Mater. At. 498 (2021) 1–8.

[53] H.K. Reynolds, et al., The Stopping Cross Section of Gases for Protons, 30-600 kev, Phys. Rev. 92 (3) (1953) 742–748.

[54] G. Schiwietz, et al., Femtosecond dynamics – snapshots of the early ion-track evolution, Nucl. Instrum. Methods Phys. Res. Sect. B Beam Interact. Mater. At. 225 (1) (2004) 4–26.

[55] J. Mbagwu, Theoretical investigation of dosimeter accuracy for linear energy transfer measurements in proton therapy: A comparative study of stopping power ratios, Radiat. Phys. Chem. 227 (2025) 112354.

[56] P.W. Atkins, J.De Paula, J. Keeler, Atkins' Physical Chemistry, Oxford University Press, 2018.

[57] G.L. Miessler, P.J. Fischer, D.A. Tarr, Inorganic Chemistry, Pearson Education, 2013.

[58] S.P.A. Sauer, J.R. Sabin, J. Oddershede, *Chapter Nine - Calculation of mean excitation energies*, in *Advances in Quantum Chemistry*. J.R. Sabin and J. Oddershede, Editors, Academic Press, 2019, pp. 225–245.

[59] J. Walkowiak, et al., Mean Excitation Energies of all ionization stages of all atoms with 1≤Z≤86, At. Data Nucl. Data Tables 161 (2025) 101696.

[60] X. Liu, et al., Establishment and validation of an electron inelastic mean free path database for narrow bandgap inorganic compounds with a machine learning approach, Phys. Chem. Chem. Phys. 25 (27) (2023) 17923–17942.

[61] P. Roussel, et al., Electronic and optical properties of plutonium metal and oxides from Reflection Electron Energy Loss Spectroscopy, Appl. Surf. Sci. 553 (2021) 149559.

[62] Nj Al-Bahnam, K.A. Ahmad, A.I.Aboo Al-Numan, Wake potential of swift ion in amorphous carbon target, Phys. Lett. A 381 (6) (2017) 616–622.

[63] Webb, R.P., *SUSPRE Software* SUSPRE software Version2.1, Surrey Ion Beam Center, Universityof Surrey: ⟨https://uknibc.co.uk/SUSPRE/publish.htm⟩.

[64] M.H.A. Mhareb, et al., Tailoring the optical, mechanical, and gamma-ray-attenuation performance of G-T-B glasses by doping nano rare-earth (Gd, Yb, Tm), Radiat. Phys. Chem. 237 (2025) 113019.